



1     **Distinctive aerosol-cloud-precipitation interactions in marine boundary layer clouds from the**  
2                                   **ACE-ENA and SOCRATES aircraft field campaigns**

3

4     Xiaojian Zheng<sup>1</sup>, Xiquan Dong<sup>1</sup>, Baike Xi<sup>1</sup>, Timothy Logan<sup>2</sup> and Yuan Wang<sup>3</sup>

5

6     <sup>1</sup>Department of Hydrology and Atmospheric Sciences, University of Arizona, Tucson, AZ, USA

7     <sup>2</sup>Department of Atmospheric Sciences, Texas A&M University, College Station, TX, USA

8     <sup>3</sup>Department of Earth System Sciences, Stanford University, Stanford, CA, USA

9

10    **Correspondence:** Xiquan Dong ([xdong@arizona.edu](mailto:xdong@arizona.edu))

11

12    **Abstract.** The aerosol-cloud-precipitating interaction within the cloud-topped Marine Boundary Layer  
13    (MBL), are being examined using aircraft in-situ measurements from Aerosol and Cloud Experiments in  
14    the Eastern North Atlantic (ACE-ENA) and Southern Ocean Clouds Radiation Aerosol Transport  
15    Experimental Study (SOCRATES) field campaigns. SOCRATES clouds have a larger number of smaller  
16    cloud droplets compared to ACE-ENA summertime and wintertime clouds. The ACE-ENA clouds,  
17    especially in wintertime, exhibit pronounced drizzle formation and growth, attributed to the strong in-  
18    cloud turbulence that enhances the collision-coalescence process. Furthermore, the Aerosol-Cloud  
19    Interaction (ACI) indices from the two aircraft field campaigns suggest distinct sensitivities. The aerosols  
20    during ACE-ENA winter are more likely to be activated into cloud droplets due to more larger aerosols  
21    and strong vertical turbulence. The enriched aerosol loading during SOCRATES generally leads to  
22    smaller cloud droplets competing for available water vapor and exhibiting a stronger ACI. The ACI  
23    calculated near the cloud base was noticeably larger than the layer-mean and near-cloud-top, owing to  
24    the closer connection between the cloud layer and sub-cloud aerosols. Notably, the sensitivities of cloud  
25    base precipitating rates to cloud-droplet number concentrations are more pronounced during the ACE-



26 ENA than during the SOCRATES campaigns. The in-cloud drizzle evolutions significantly alter sub-  
27 cloud cloud condensation nuclei (CCN) budgets through the coalescence-scavenging effect, and in turn,  
28 impact the ACI assessments. The results of this study can enhance the understanding and aid in future  
29 model simulation and assessment of the aerosol-cloud interaction.

30

31

## 32 **1. Introduction**

33 Marine boundary layer (MBL) clouds substantially impact the Earth's climate system (Dong and  
34 Minnis, 2022). Sustained by large-scale subsidence and cloud-top longwave radiative cooling, MBL  
35 clouds, typically located beneath the temperature inversion at the MBL top, persistently reflect the  
36 incoming solar radiation and modulate the radiative balance (Lilly, 1968; Albrecht et al., 1995; Wood et  
37 al., 2015; Dong et al., 2023). The climatic significance of MBL cloud radiative effects, which remains  
38 largely uncertain (IPCC, 2022), is closely linked to cloud microphysical properties that are substantially  
39 influenced by surrounding aerosol conditions (Chen et al., 2014; Feingold and McComiskey, 2016).  
40 Observational evidence demonstrates that cloud microphysical responses to aerosols, defined as the  
41 aerosol-cloud interaction (ACI), can be typically viewed as decreased cloud droplet effective radii ( $r_c$ )  
42 and increased number concentrations ( $N_c$ ) under an augmented aerosol intrusion. The ACIs have been  
43 extensively investigated by different observational platforms, such as aircraft, ground-based and satellite  
44 observations, and model simulations over different maritime regions (Hill et al., 2009; Diamond et al.,  
45 2018; Painemal et al., 2020; Wang et al., 2020; Zheng et al., 2022a).

46 Furthermore, more and smaller cloud droplets not only extend cloud longevity and spatial  
47 coverage but also modulate the precipitation processes, reflecting the cloud adjustments to aerosol  
48 disturbances (Albrecht, 1989; Bellouin et al., 2020). Since precipitation is common in MBL clouds,  
49 particularly in the form of drizzle (Wood et al., 2015; Wu et al., 2020), the formation and growth of  
50 drizzle drops are deeply entwined with the MBL aerosols and turbulence. On the one hand, aerosols have



51 been found to suppress the precipitation frequency and strength by constantly buffering cloud droplet  
52 number concentrations via activation, hence increasing cloud precipitation susceptibility (Lu et al., 2009;  
53 Sorooshian et al., 2009; Duong et al., 2011). On the other hand, in-cloud turbulence and wind shear can  
54 effectively enhance collision-coalescence efficiency, stimulating drizzle formation and growth, and  
55 consequently leading to enhanced precipitation (Chen et al., 2011; Wu et al., 2017). Conversely,  
56 precipitation has been shown to induce a substantial influence on the MBL aerosol and cloud  
57 condensation nuclei (CCN) budget, via the coalescence-scavenging effect. As the drizzle drops descend,  
58 they are enlarged by collecting more cloud droplets within the cloud layer. However, the drizzle drops,  
59 once falling out of the cloud base, can result in net reductions in sub-cloud aerosols and CCN budgets  
60 via the coalescence-scavenging effect (Wood, 2006; Zheng et al., 2022b). Quantitative estimates of these  
61 effects remain ambiguous and inconclusive, which is subject to multiple factors such as aerosol  
62 physicochemical characteristics, cloud morphology, and MBL dynamics and thermodynamics conditions  
63 (Sorooshian et al., 2009; Duong et al., 2011; Diamond et al., 2018; Brunke et al., 2022). Thus, more  
64 studies on the aforementioned processes regarding MBL aerosols and clouds over different maritime  
65 regions are warranted to pursue an in-depth understanding of aerosol-cloud-precipitation interactions  
66 (ACPIs).

67 The Eastern North Atlantic (ENA) stands as a desirable region for exploring MBL clouds in the  
68 mid-latitude, with Graciosa Island in the Azores (39.09°N, 28.03°W) representing a focal point for such  
69 studies. Located between the mid-latitude and subtropical climate zones, Graciosa is subject to the  
70 meteorological influence of both the Icelandic Low and the Azores High, and the influence of aerosols  
71 ranging from pristine marine air masses to those heavily influenced by continental emissions from North  
72 America and Northern Europe (Logan et al., 2014; Wood et al., 2015; Wang et al., 2020). Addressing  
73 the need for sustained research into the MBL clouds, the recent Aerosol and Cloud Experiments in the  
74 Eastern North Atlantic (ACE-ENA) aircraft campaign (J. Wang et al., 2022) were conducted in the  
75 summer 2017 (ACEENA Sum) and winter 2018 (ACEENA Win). During these two intensive operation



76 periods (IOPs) of ACE-ENA, the research aircraft accrued abundant in-situ measurements of aerosols,  
77 clouds, and drizzle properties, providing invaluable resources for studying the ACI and ACPI processes.

78 Over the Southern Ocean (SO), the Southern Ocean Clouds Radiation Aerosol Transport  
79 Experimental Study (SOCRATES) field campaign (McFarquhar et al., 2021) was conducted during the  
80 austral summer, which marks another valuable piece of the MBL cloud research. The SO, being one of  
81 the cloudiest regions globally, is predominantly influenced by naturally produced aerosols originating  
82 from oceanic sources due to its remoteness, where the anthropogenic and biomass burning aerosols exert  
83 minimal influence over the region (McCoy et al., 2021; Sanchez et al., 2021; Twohy et al., 2021; Zhang  
84 et al., 2023). The aerosol budget in this region is primarily shaped by biological aerosols, which nucleate  
85 from the oxidation products of dimethyl sulfide (DMS) emissions, as well as by sea spray aerosols. Hence,  
86 the SO provides an unparalleled natural laboratory for discerning the influence of these natural aerosol  
87 emissions on the MBL clouds. Furthermore, the MBL clouds over the SO predominantly consist of  
88 supercooled liquid water droplets, which coexist with mixed- and ice-phase processes (Y. Wang et al.,  
89 2021a; Xi et al., 2022), while the precipitation phases are examined to be primarily dominated by liquid  
90 hydrometeors (Tansey et al., 2022; Kang et al., 2023). The in-situ measurements collected from  
91 SOCRATES have cultivated numerous studies on aerosols, clouds, and precipitation over the SO using  
92 both in-situ measurements and model simulations (McCoy et al., 2020; Altas et al., 2021; D'Alessandro  
93 et al., 2021), and provides an opportunity to study the liquid cloud processes under a colder nature.

94 This study examines the similarities and differences in the MBL aerosol, cloud, drizzle properties,  
95 their distribution and evolution, and their ACIs and ACPIs from selected cloud cases during ACE-ENA  
96 and SOCRATES. The data and methods used in this study are introduced in section 2. The aerosol and  
97 CCN properties in the above- and sub-cloud regimes, and the vertical distributions of MBL cloud and  
98 drizzle properties are examined in section 3. The ACI, precipitation susceptibility and drizzle impacts on  
99 the sub-cloud aerosols and CCN (ACPI) are discussed in section 4. Finally, the findings are summarized  
100 along with the discussions of the importance of this study in section 5.



101 **2. Data and methods**

102 **2.1 Cloud and drizzle properties**

103 The in-situ measurements of MBL cloud properties are temporally synchronized to 1 Hz  
104 resolution, corresponding to approximately 100 m (5 m) of horizontal (vertical) sampling. The Fast Cloud  
105 Droplet Probe (FCDP) onboard aircraft during ACE-ENA can detect droplets with diameter ( $D_p$ ) ranging  
106 from 1.5  $\mu\text{m}$  to 50  $\mu\text{m}$  at resolutions between 1 and 3  $\mu\text{m}$  (Glienke and Mei, 2020), while the SOCRATES  
107 used a similar CDP to measure droplets from 2  $\mu\text{m}$  to 50  $\mu\text{m}$  at a 2  $\mu\text{m}$  resolution. Both ACE-ENA and  
108 SOCRATES leverage the Two-Dimensional Stereo Particle Imaging Probe (2DS) to discern droplets  
109 with diameters from 5  $\mu\text{m}$  to 1280  $\mu\text{m}$  (Lawson et al., 2006; Glienke and Mei, 2019). The 2DS in-situ  
110 measurements will be used as additional screening to eliminate large ice particles ( $D_p > 200 \mu\text{m}$ ).  
111 Moreover, the University of Washington Ice–Liquid Discriminator product, which is a Machine-  
112 learning-based single-particle phase classification of the 2DS images, is used to identify small ice crystals  
113 when available. Through these three datasets, we can tease out the ice-dominated period to the utmost  
114 extent and focus on the liquid cloud processes and ACI during the SOCRATES (Atlas et al., 2021; Wang  
115 et al., 2021).

116 Although these in-situ measurements can provide “ground-truth” datasets, their uncertainties  
117 must be properly analyzed and data quality must be controlled before being applied to scientific studies.  
118 The uncertainties of FCDP in sizing and concentration are approximately 30% and 20%, respectively  
119 (Baumgardner et al., 2017). Considering the significant uncertainty in the concentration of smaller  
120 particles from a photodiode probe such as 2DS (Baumgardner & Korolev, 1997; Wang et al., 2021), a  
121 diameter of 40  $\mu\text{m}$  is used as the demarcation line between cloud droplets and drizzle drops (Wood et al.,  
122 2005). Then droplet number concentrations in the overlapping size bin between FCDP and 2DS are  
123 redistributed assuming a gamma distribution, thereby a complete size spectrum of cloud and drizzle can



124 be merged from FCDP and 2DS measurements. Hence, the cloud and drizzle microphysical properties  
125 can be calculated.

126 The cloud droplet number concentration ( $N_c$ ) is given by:

$$127 \quad N_c = \int_2^{40} n(D_p) dD_p, \quad (1)$$

128 The cloud droplet effective radius ( $r_c$ ) is given by:

$$129 \quad r_c = \frac{\int_2^{40} r_p^3 n(D_p) dD_p}{\int_2^{40} r_p^2 n(D_p) dD_p}, \quad (2)$$

130 The cloud liquid water content ( $LWC_c$ ) can be calculated by:

$$131 \quad LWC_c = \frac{4}{3} \pi \rho_w \int_2^{40} D^3 n(D_p) dD_p, \quad (3)$$

132 where  $\rho_w$  is water density.

133 Similarly, the drizzle drop number concentration ( $N_d$ ) and liquid water content ( $LWC_d$ ) can be calculated  
134 using the size distribution from 40  $\mu\text{m}$  to 1280  $\mu\text{m}$ . Particularly, the drizzle mean mass diameter ( $D_{mmd}$ )  
135 is given by:

$$136 \quad D_{mmd} = \left( \frac{\int_{40}^{1280} D_p^3 n(D_p) dD_p}{\int_{40}^{1280} n(D_p) dD_p} \right)^{1/3}, \quad (4)$$

137 This quantity is chosen because the  $D_{mmd}$  denotes the diameter of average mass (the third-moment  
138 average) of the drizzle size distribution, which provides the link between the number concentration and  
139 the mass concentration of drizzle droplets in a sample (Hinds, 1999).

140 Adapting the method in Zheng et al. (2022b), the cloud base precipitation rate ( $R_{CB}$ ) is given by:

$$141 \quad R_{CB}(\text{mm/hr}) = 6\pi * 10^{-4} \int_{40\mu\text{m}}^{1280\mu\text{m}} D_{p,mm}^3 n(D_{p,mm}) U_\infty(D_{p,mm}) dD_{p,mm}, \quad (5)$$

142 in order to match the unit conversion, the  $D_{p,mm}$  is diameter in unit of mm,  $n(D_{p,mm})$  is drizzle number  
143 concentration in every size bin with a unit of  $\# \text{ m}^3 \text{ mm}^{-1}$ , and  $U_\infty(D_{p,mm})$  is terminal velocity in given  
144 size bin, which is calculated from the full Reynolds number theory as in Pruppacher and Klett (2010).



145           The combined threshold of  $N_c > 5 \text{ cm}^{-3}$  and  $LWC_c > 0.01 \text{ g m}^{-3}$  is used for determining the valid  
146 cloud samples and cloud boundaries (Wood, 2005; Zheng et al., 2022b). The complete cloud vertical  
147 profiles from sub-cloud to the above-cloud are selected during the ACE-ENA and SOCRATES IOPs, in  
148 which the flight strategy includes sawtooth and spiral cloud transects and ramping cloud sampling. The  
149 precipitation conditions are determined by whether samples of  $N_d > 0.001 \text{ cm}^{-3}$  exists below the cloud  
150 base height. In total, the selected numbers of cloud (precipitating cloud) profiles are 18 (13), 26 (13), and  
151 28 (24) for ACE-ENA summer and winter IOPs along with SOCRATES, respectively. The detailed  
152 selected cloud profiles are listed in Table S1, along with the cloud profile macrophysics. Additionally,  
153 for the purposes of studying the sub-cloud aerosols that actually interact with the cloud, the sub-cloud  
154 mixed layer is determined following the threshold suggested by Jones et al. (2011). Starting from the  
155 cloud base and looking downward, the mixed layer altitude is defined as where the vertical changes in  
156 liquid water potential temperature ( $\theta_L$ ) and total water mixing ratio ( $q_t$ ) exceed 0.5 K and 0.5 g/kg,  
157 respectively. Hence, the mixed layer thickness is defined as the difference in cloud top altitude and mixed  
158 layer altitude. An example of the mixed layer identification is shown in Figure S1. The sub-cloud aerosols  
159 are thus selected between the mixed layer altitude and cloud base in order to best represent the aerosol-  
160 cloud interactions, while the above-cloud aerosols are selected between the cloud top and 200 m above  
161 (Wang et al., 2020).

## 162 **2.2 Aerosol properties**

163           The total aerosol number concentrations ( $N_a$ ) from ACE-ENA and SOCRATES are measured by  
164 the airborne Condensation Particle Counter (CPC) models 3772 and 3760A, which counts the number of  
165 aerosols with diameter ( $D_p$ ) larger than 3 nm and 11 nm, respectively (Kuang and Mei, 2019;  
166 SOCRATES Low Rate Data, 2022). Additionally, the Passive Cavity Aerosol Spectrometer (PCASP)  
167 onboard the ACE-ENA aircraft is capable of sizing the aerosol with  $D_p$  ranging from 0.1  $\mu\text{m}$  to 3.2  $\mu\text{m}$   
168 (Goldberger, 2020). While the ultra-high sensitivity aerosol spectrometer (UHSAS) measures the size-



169 resolved aerosol distribution from 0.06  $\mu\text{m}$  to 1.0  $\mu\text{m}$  during SOCRATES (Uin, 2016). Therefore, the  
170 number concentrations of accumulation mode aerosols ( $N_{ACC}$ , 0.1  $\mu\text{m}$ -1  $\mu\text{m}$ ) can be discerned from the  
171 PCASP and UHSAS aerosol size distributions. The Aitken mode aerosols ( $N_{Ait}$ ,  $< 0.1 \mu\text{m}$ ) from the  
172 ACE-ENA is given by the fast integrated mobility spectrometer (FIMS), which can size the aerosol down  
173 to 9 nm (Olfert et al., 2008), while the  $N_{Ait}$  from SOCRATES is limited to 0.06  $\mu\text{m}$  – 0.1  $\mu\text{m}$  due to the  
174 limitation of UHSAS. As for the CCN measurements, the ACE-ENA utilized the Dual-Column CCN  
175 Counter at two constant supersaturation levels of 0.15% and 0.35% (Uin and Mei, 2019), while the CCN  
176 number concentration ( $N_{CCN}$ ) during SOCRATES was measured under various supersaturation levels  
177 from 0.06% to 0.87% using a scanning CCN counter (Roberts and Nenes, 2005). In this study,  $N_{CCN}$  at  
178 0.35% supersaturation ( $N_{CCN0.35\%}$ ) is used to ensure a direct comparison between ACE-ENA and  
179 SOCRATES. The aerosol measurements are in the temporal resolution of 1Hz. Note that the aerosol and  
180 CCN data are quality-controlled by removing the data point where the  $N_c + N_d$  greater than 5  $\text{cm}^{-3}$  or  $N_d$   
181 greater than 0.01  $\text{cm}^{-3}$ , to filter out the contamination of the cloud droplets, and drizzle water splashing.

182

### 183 **3. Aerosol, cloud, and drizzle properties of selected cases**

#### 184 **3.1 Aerosols and CCN in above- and sub-cloud regimes**

185 The probability density functions (PDFs) of aerosols, CCN, and cloud microphysical properties  
186 from selected cases during the ACE-ENA and SOCRATES field campaigns are presented in Figure 1.  
187 Notably, the  $N_a$ ,  $N_{ACC}$  and  $N_{CCN0.35\%}$  values from the SOCRATES are the highest among the three IOPs,  
188 followed by the ACE-ENA summer and winter as illustrated in both above-cloud (Figs. 1a-1c) and sub-  
189 cloud regimes (Figs. 1d-1f). Such variations can be linked to the disparate aerosol sources in the ACE-  
190 ENA and SOCRATES regions, especially during the summer and winter seasons over the Azores.

191 In the SOCRATES region, dominant air masses primarily originate from the south or from the  
192 west, skirting the Antarctic coast (Zhang et al., 2023). The SOCRATES above-cloud aerosols (674.6  $\text{cm}^{-3}$





193 <sup>3</sup>) are primarily constituted by the Aitken mode aerosols because the mean  $N_{Acc}$  is only  $62.5 \text{ cm}^{-3}$ . These  
194 aerosols are predominantly produced from the oxidation of biogenic gases, notably the dimethyl sulfide  
195 (DMS) emitted by marine biological productivity (Sanchez et al., 2018; McCoy et al., 2020). Conversely,  
196 the ENA region experiences aerosols of varied origins, spanning maritime air masses to those heavily  
197 influenced by continental emissions from North America or Northern Europe (Logan et al., 2014; Wang  
198 et al., 2020). During the summer ACE-ENA campaign, the MBL is enriched by sulfate and carbonaceous  
199 particles (Y. Wang et al., 2021b; Zawadowicz et al., 2021). This enhancement is attributed both to local  
200 generation from DMS and to the long-range transport from the continental air masses, resulting in the  
201 mean  $N_a$  of  $312.6 \text{ cm}^{-3}$  and  $301.5 \text{ cm}^{-3}$  for above- and sub-cloud regimes, respectively. The ACE-ENA  
202 winter exhibits the lowest aerosol and CCN concentrations, predominantly sourced from local maritime  
203 influences, and coupled with reduced continental air mass intrusions (Zheng et al., 2018; Y. Wang et al.,  
204 2021b).

205 Figure 1a reveals that there are more above-cloud  $N_a$  during the three IOPs than sub-cloud values,  
206 especially during the SOCRATES. The higher above-cloud  $N_a$  values from the three IOPs are primarily  
207 contributed by Aitken mode aerosols because their corresponding  $N_{Acc}$  values are much lower (Figs.  
208 1a&b). It is interesting to note that the above-cloud  $N_{CCN0.35\%}$  values exceed the  $N_{Acc}$  for all three IOPs  
209 (Figs. 1b&c), implying that a significant fraction of Aitken mode aerosols can be activated to become  
210 CCN, corroborating findings from earlier studies (McCoy et al., 2021; Zheng et al., 2021). For the sub-  
211 cloud regime, the  $N_a$  values during SOCRATES and ACE-ENA winter are ~70-80% of their  
212 corresponding above-cloud values, and the  $N_a$  during ACE-ENA summer is almost identical to its above-  
213 cloud value. Notice that the  $N_{Acc}$  values from three IOPs are more than doubled their above-cloud values,  
214 and most of them can be activated to become CCN at SS of 0.35%. It is interesting to note that the higher  
215  $N_{CCN0.35\%}$  at sub-cloud layer during SOCRATES may partially result from the cloud process on aerosols



216 (Figs. 1e&f), which is suggested by previous studies (McCoy et al., 2021; Zhang et al., 2023), and will  
217 be further discussed.

218 To further investigate the above- and sub-cloud aerosol properties from three IOPs, the aerosol  
219 droplet size distributions are analyzed in Figure 2. It is evident that SOCRATES aerosols have the highest  
220 concentrations of Aitken mode particles ( $D_p = 0.06 - 0.1 \mu\text{m}$ , given that the  $< 0.06 \mu\text{m}$  is not available  
221 from UHSAS) for both the above- and sub-cloud regimes. McCoy et al. (2021) and Zheng et al. (2021)  
222 identified analogous origins and formations of the above-cloud Aitken mode aerosols over both the SO  
223 and ENA regions and concluded that these aerosols primarily originate from the nucleation of photo-  
224 oxidation products of DMS, notably  $\text{H}_2\text{SO}_4$  and MSA, in the free troposphere (FT). The differential  
225 concentrations can be ascribed to the fact that sea-surface DMS concentrations in the SO are generally  
226 higher than those in the ENA region (Aumont et al., 2002; Zhang et al., 2023). Moreover, DMS emissions  
227 in the ENA during summer surpass those during winter (Zawadowicz et al., 2021). For the accumulation  
228 mode aerosols ( $0.1 - 1 \mu\text{m}$ ), the  $N_{Acc}$  values for both above- and sub-cloud regimes during SOCRATES  
229 decrease monotonically with particle size. The results in Figure 2 further support the finding that Aitken  
230 mode aerosols are dominant over the SO. The  $N_{Acc}$  values during ACE-ENA show slight uplifts for the  
231 small accumulation mode aerosols ( $< 0.3 \mu\text{m}$ ), particularly for summer, reflecting the signal of potential  
232 long-range transport of fine-mode aerosols (Wang et al., 2020; Y. Wang et al., 2021b). Consequently,  
233 such comparison reinforces the notion that the SO represents a largely pre-industrial marine environment,  
234 wherein the influence of anthropogenic and biomass-burning aerosols is minimal (McCoy et al., 2020,  
235 2021; Zhang et al., 2023).

236 When contrasting the aerosol size distributions in the sub-cloud regime (Fig. 2b) with those in the  
237 above-cloud regime, the influence of cloud processing on aerosols is discernibly non-trivial, particularly  
238 under the cloud-topped MBL conditions examined in this study. While the FT aerosols can be further  
239 entrained down and contribute to the population of Aitken mode aerosols within the MBL, the sub-cloud



240 aerosols can also be subject to the influence of new particle formation in the upper MBL, though arguably  
241 less effective than those within the FT (Zheng et al., 2021). Additionally, in-cloud Brownian capture can  
242 lead to a substantial reduction in Aitken mode aerosols (Hudson et al., 2015; Wyant et al., 2022),  
243 providing the rationale for the observed decrease in Aitken mode aerosols in the sub-cloud regime,  
244 especially for particles smaller than  $0.07 \mu\text{m}$ . In addition, cloud chemical processing, such as the  
245 aqueous-phase condensation of sulfuric acid onto the aerosol cores inside the cloud droplets, is  
246 particularly pronounced during the transitioning of Aitken mode aerosols to accumulation mode aerosols  
247 (Hudson et al., 2015; Zhang et al., 2023).

248 From both above- to sub-cloud regimes, the larger Aitken mode aerosols ( $> 0.07 \mu\text{m}$ ) can be  
249 effectively enlarged to accumulation mode aerosols through coagulation and water vapor diffusional  
250 growth (Covert et al., 1996), contributing to the elevated accumulation mode aerosol distribution and  
251 increased  $N_{Acc}$  in the sub-cloud regime. These processes are particularly evidenced by the decrease of  
252 critical supersaturations from above-cloud (between 0.35% - 0.4%) to sub-cloud (between 0.3% - 0.35%)  
253 during SOCRATES (Fig. S2) because the aerosol droplet sizes are enlarged and more readily become  
254 CCN. Furthermore, the in-cloud coalescence process combines mixtures of large and small cloud droplets,  
255 and results in the sub-cloud aerosol residuals shifting towards the larger size, upon the droplet  
256 evaporation below the cloud (often manifested as drizzle). This partially elucidates the observed increase  
257 in the tail-end of the accumulation mode aerosol distribution for all three IOPs. The elevation in sub-  
258 cloud coarse mode aerosols observed for both ACE-ENA IOPs (as seen in Fig. S3) can be attributed both  
259 to the coalescence-enlargement process as well as the intrusion of marine aerosols (e.g., sea salt).

260

### 261 **3.2 Bulk cloud microphysical properties distribution**

262 The PDFs of MBL cloud microphysical properties ( $N_c$ ,  $r_c$ ,  $LWC_c$ ) derived from aircraft in-situ  
263 measurements from the three IOPs are shown in Figures 1g-1i. The mean microphysical properties for  
264 the individual cloud profiles are listed in Table S2. The results in Figure 1 have demonstrated that



265 aerosol/CCN sources and concentrations, especially from the sub-cloud regime, play an important role  
266 in cloud droplet formation and evolution. For example, the SOCRATES has the highest sub-cloud  
267 aerosols and CCN, and subsequently feature a larger number of smaller cloud droplets, given the highest  
268  $N_c$  ( $148.3 \text{ cm}^{-3}$ ) and smallest  $r_c$  ( $8 \text{ }\mu\text{m}$ ) among the three IOPs. These results have further improved the  
269 understanding of the aerosol first indirect effect: more aerosols induce more smaller cloud droplets  
270 (higher  $N_c$  and smaller  $r_c$ ) under the constrained liquid water content conditions, thus the MBL clouds  
271 reflect more incoming solar radiation (Twomey, 1977). The ACE-ENA wintertime clouds feature the  
272 fewest  $N_c$  ( $70.6 \text{ cm}^{-3}$ ) and largest  $r_c$  ( $9.8 \text{ }\mu\text{m}$ ), while the  $N_c$  and  $r_c$  ( $89.4 \text{ cm}^{-3}$  and  $9 \text{ }\mu\text{m}$ ) during ACE-  
273 ENA summer fall between the SOCRATES and ACE-ENA winter values. Considering the aerosol  
274 competing effect against the available water vapor, the relatively abundant aerosols in SOCRATES might  
275 account for the narrower  $r_c$  distribution, which peaks between  $6 - 10 \text{ }\mu\text{m}$ . SOCRATES has a lower cloud-  
276 layer water vapor mixing ratio (figure not shown) compared to ACE-ENA because the SO region has  
277 been observed to contain less precipitable water vapor than the ENA region due to the colder sea surface  
278 temperatures (Marcovecchio et al., 2023). Therefore, the aerosol and cloud properties in Figure 1 promise  
279 further examination of different cloud microphysical responses to aerosols via the ACI process. Note that  
280 the  $N_{CCN0.35\%}$  values are less than  $N_c$  values during the ACE-ENA winter IOP, thereby offering  
281 compelling further investigation on potential impacts of precipitation on the MBL CCN budget. These  
282 aerosol-cloud-precipitation interactions (ACPIs) will be discussed in Section 4.

283

### 284 **3.3 Vertical distributions of cloud and drizzle microphysics**

285 The vertical distributions of the cloud and drizzle microphysical properties within the cloud layer  
286 from the three IOPs are shown in Figure 3. To ensure the representative vertical profiles, all the in-cloud  
287 samples are vertically smoothed by using a triangular moving average method, and are inverse distance  
288 weighted in every 50 m moving altitude windows. Furthermore, the altitude is then normalized by  $z_i =$



289  $\frac{z - z_{base}}{z_{top} - z_{base}}$ , where  $z_i = 0$  denotes cloud base and  $z_i = 1$  denotes cloud top. Consistent with previous  
290 discussions on the bulk microphysics distribution, the mean  $N_c$  values from SOCRATES are consistently  
291 higher than ACE-ENA summer and winter for the entire cloud layer, with a slight increase ranging from  
292 the cloud base to the upper-middle part ( $z_i \approx 0.85$ ) and then decreasing toward the cloud top due to  
293 cloud-top entrainment (Fig. 3a). All  $r_c$  values from the three IOPs show a near-linear increase from cloud  
294 base to top, with the smallest values observed during SOCRATES and the largest values observed during  
295 ACE-ENA winter (Fig. 3b).

296 The warmer and drier air near the cloud top entrained into the cloud layer and further mixing  
297 downward often results in the evaporation of small cloud droplets and the shrinking of droplet sizes  
298 which oppose condensational growth (Desai et al., 2021). Decreases in both  $N_c$  and  $LWC_c$ , and the  
299 reduced growth of  $r_c$  near the cloud top ( $z_i > 0.85$ ) support signals of cloud-top entrainment mixing  
300 during all three IOPs. It is interesting to note that the  $r_c$  values from SOCRATES increase monotonically  
301 from cloud base to top, while the  $r_c$  values from both ACE-ENA summer and winter increase until  $z_i \approx$   
302 0.8 and then remain nearly constant, although all of their  $N_c$  values (at  $z_i \approx 0.8$ ) decrease towards the  
303 cloud top. When dry air entrainment occurs at the cloud top, some of the upper-level smaller cloud  
304 droplets will evaporate, which provides an extra water vapor source and leads to decreases in  $N_c$  (Fig.  
305 3a). This extra water vapor can then be re-condensed on the cloud droplets and potentially enlarge the  
306 droplet size. This effect is more pronounced on smaller cloud droplets since there is a smaller surface  
307 area (Wallace and Hobbs, 2006), as shown in the continuous growth of  $r_c$  during SOCRATES. On the  
308 other hand, the cloud-top entrainment mixing can shrink the large cloud droplets via evaporation. The  
309 nearly constant  $r_c$  values (at  $z_i > 0.8$ ) represents the balance of these two competing processes. The  
310 impact of these two processes on cloud droplets depends on the cloud-top entrainment mixing rate.

311 While carrying the distinct discrepancies in the mean values for all layers, the  $N_c$  and  $r_c$  from ACE-  
312 ENA summer and winter clouds experienced similar vertical evolutions as the SOCRATES. The



313 increases of  $r_c$  ( $\Delta r_c$ ) from cloud base to cloud top are 4.03  $\mu\text{m}$ , 4.78  $\mu\text{m}$  and 5.85  $\mu\text{m}$  for SOCRATES,  
314 ACE-ENA summer and winter, respectively. Consequently, the  $LWC_c$  values from the three IOPs are  
315 comparable to each other. The vertical distributions of MBL cloud microphysical properties examined  
316 in this study are in good agreement with the previous studies conducted on these two field campaigns  
317 (Wu et al., 2020a; Y. Wang et al., 2021a; J. Wang et al., 2021; Wang et al., 2023). In addition, the cloud  
318 adiabaticity is defined as  $f_{ad} = LWC_c/LWC_{ad}$ , where the  $LWC_{ad}$  denotes adiabatic LWC (Wu et al.,  
319 2020b). As shown in Figure S4, the clouds from all three IOPs feature certain levels of sub-adiabaticity  
320 above the cloud base. The layer-mean  $f_{ad}$  values are  $0.681 \pm 0.083$ ,  $0.476 \pm 0.106$ , and  $0.447 \pm 0.100$  for  
321 SOCRATES, ACE-ENA summer and winter, respectively. It has been well known that the cloud sub-  
322 adiabaticity is primarily induced by the in-cloud collision-coalescence and the entrainment mixing  
323 processes (Hill et al., 2009; Braun et al., 2018; Gao et al., 2020; Wu et al., 2020b).

324 To quantitatively evaluate the impact of cloud-top entrainment mixing rate on cloud droplets, we  
325 adapt the method of Albrecht et al. (2016), where the cloud-top entrainment rate ( $w_e$ ) can be expressed  
326 as

$$327 \quad w_e = A_\sigma * \sigma_w / R_{i\sigma} , \quad (6)$$

328 where the turbulence kinetic energy (TKE) dissipation coefficient  $A_\sigma$  is empirically taken as 26 as in  
329 Albrecht et al. (2016), and the  $R_{i\sigma}$  is the buoyancy Richardson number calculated by  $(g/\theta_0) * (\Delta\theta_v h / \sigma_w^2)$ .  $\sigma_w$  denotes the standard deviation of vertical velocities taken near the cloud top ( $z_i > 0.9$ ),  
330 and  $h$  is the MBL height.  $\theta_0$  is the reference potential temperature and  $\Delta\theta_v$  is the virtual potential  
331 temperature difference across the temperature inversion layer above the cloud. Given the valid vertical  
332 velocity measurements for the selected cloud cases, the averaged  $w_e$  values are  $0.570 \pm 0.834 \text{ cm s}^{-1}$ ,  
333  $0.581 \pm 0.560 \text{ cm s}^{-1}$ , and  $0.960 \pm 1.127 \text{ cm s}^{-1}$  for SOCRATES, ACE-ENA summer and winter,  
334 respectively. The stronger  $w_e$  during ACE-ENA winter might be induced by the generally weaker cloud-  
335 top inversions and stronger near-cloud top turbulence, compared to the summertime when the ENA is  
336



337 dominated by the large-scale high-pressure system (Ghate et al., 2021). Considering the near cloud-top  
338 proportion of cloud where the  $LWC_c$  experienced decrease, the reduction of  $LWC_c$  for the ACE-ENA  
339 summer ( $-0.032 \text{ g m}^{-3}$ ) is higher than the reductions in winter ( $-0.018 \text{ g m}^{-3}$ ) and SOCRATES ( $-0.009 \text{ g}$   
340  $\text{m}^{-3}$ ), albeit that the  $w_e$  for ACE-ENA summer is comparable to SOCRATES, and much lower than ACE-  
341 ENA winter values. Within the above-cloud inversion layer, the temperature (water vapor mixing ratio)  
342 differences  $\Delta T$  ( $\Delta q$ ) are  $1.76 \text{ K}$  ( $-1.75 \text{ g kg}^{-1}$ ),  $1.54 \text{ K}$  ( $-1.66 \text{ g kg}^{-1}$ ) and  $1.48 \text{ K}$  ( $-1.09 \text{ g kg}^{-1}$ ) for  
343 SOCRATES, ACE-ENA summer and winter, respectively. Therefore, the warmer and dryer entrained  
344 air can partially contribute to the greater  $LWC_c$  reduction and the lower  $f_{ad}$  (0.39) during the ACE-ENA  
345 summer than those during the ACE-ENA winter ( $f_{ad} = 0.45$ ) and SOCRATES ( $f_{ad} = 0.66$ ) near the  
346 cloud top (Fig. S4).

347 Figures 3d-3f illustrate the normalized profiles of MBL drizzle microphysical properties. The  $N_d$   
348 values from the three IOPs mimic each other, which all maximize at the cloud top and then monotonically  
349 decrease toward the cloud base (Fig. 3d), while their  $LWC_d$  values follow a similar trend, albeit with  
350 relatively large differences (Fig. 3f). In contrast to the  $N_d$  and  $LWC_d$  trends, the  $D_{mmd}$  gradually increase  
351 from cloud top to cloud base (Fig. 3e), making physical sense since the drizzle droplets are typically  
352 formed near cloud top and continuously grow via collision-coalescence process while falling. The ACE-  
353 ENA wintertime drizzle  $D_{mmd}$  and  $LWC_d$  are distinctively larger than those in summertime and  
354 SOCRATES. It is interesting to note that near the cloud top ( $z_i > 0.9$ ), the ACE-ENA winter has  
355 comparable  $N_d$  but much larger  $D_{mmd}$  than the other two IOPs, suggesting that there were more large  
356 drizzle embryos formed from large cloud droplets (Fig. 3b) during ACE-ENA winter.

357 In order to further analyze the cloud-to-drizzle conversion processes, the cloud and drizzle droplet  
358 size distributions (DSD) are categorized into four segments based on their relative position within the  
359 cloud layer (Fig. 4): upper cloud ( $z_i > 0.8$ , Fig. 4a), upper-middle cloud ( $0.5 \leq z_i < 0.8$ , Fig. 4b), lower-  
360 middle cloud ( $0.2 \leq z_i < 0.5$ , Fig. 4c) and lower cloud ( $z_i < 0.2$ , Fig. 4d). The cloud DSDs ( $D_p < 40$



361  $\mu\text{m}$ ) from the three IOPs gradually shift towards larger sizes, moving from the lower to the upper cloud  
362 regions. This is accompanied by the narrowing of the DSD ranges, as evidenced by the decline in the  
363 cloud relative dispersion ( $\epsilon$ ). The relative dispersion of cloud droplets ( $\epsilon$ ) is a parameter that represents  
364 the DSD and is defined as the ratio between the standard deviation and the mean radius of the distribution.  
365 At the lower portion of the cloud (Fig. 4d), the relatively greater value of  $\epsilon$  clearly represents the co-  
366 existence of the newly formed small cloud droplets from recently activated CCNs and the sedimentation  
367 of larger droplets from the upper sections of the cloud. In addition, the discrepancies in  $\epsilon$  between the  
368 three IOPs may be attributed to the sub-cloud aerosol differences, as Y. Wang et al. (2021a) stated that  
369 the higher aerosol loading leads to increased  $\epsilon$  due to the water vapor competition effect.

370 Notably, the cloud DSDs during ACE-ENA winter exhibit a more pronounced negative skew (to the  
371 left) than those during ACE-ENA summer, possibly due to the activation of more sub-cloud coarse mode  
372 aerosols to become larger cloud embryos, as demonstrated in Fig. S3. Ascending within the cloud, the  
373 process of water vapor condensation perpetually pushes the DSD towards larger sizes, culminating in a  
374 more negatively skewed DSD. Concurrently, the cloud-top entrainment mixing plays a pivotal role in  
375 minimizing  $\epsilon$  in the upper cloud region, as elaborated by Lu et al. (2023). Note that in the upper region  
376 of the cloud (Fig. 4a), the ACE-ENA winter clouds contain more cloud droplets close to  $40 \mu\text{m}$ , albeit  
377 the mean  $N_c$  is lower. This scenario is conducive to the formation of larger drizzle embryos compared to  
378 summertime clouds, as depicted in Fig. 3e. In comparison, the SOCRATES clouds feature a pronounced  
379 log-normal DSD than the ACE-ENA, as the DSDs peak at  $D_p \sim 15 \mu\text{m}$  throughout the cloud, and  
380 subsequently, the lack of larger cloud droplets resulted in the smaller drizzle embryos near the cloud top.  
381 As the newly formed drizzle drops descend and continuously grow through the collision-coalescence  
382 process, the drizzle DSDs ( $D_p > 40 \mu\text{m}$ ) are noticeably broadened. From upper to lower cloud regions,  
383 the longer tails of the drizzle DSDs expand at the cost of smaller drizzle drops and cloud droplets via the  
384 collision-coalescence process. The clouds observed during ACE-ENA, especially in wintertime, contain





385 more large drizzle drops ( $D_p > 200 \mu\text{m}$ ) than SOCRATES, which is reflected in the distinct differences  
386 in the vertical  $D_{mmd}$  as shown in Fig. 3e.

387 It has been intensively studied that in-cloud turbulence can stimulate collision-coalescence and  
388 consequently enhance the drizzle evolution processes (Pinsky et al., 2007; Grabowski and Wang, 2013;  
389 Wu et al., 2017; Chen et al., 2018). The turbulence strength is characterized by the turbulence kinetic  
390 energy (TKE), which is calculated as:

$$391 \quad TKE = \frac{1}{2}(\overline{u'^2} + \overline{v'^2} + \overline{w'^2}), \quad (7)$$

392 where the turbulent perturbations of vertical ( $\overline{w'^2}$ ) and horizontal ( $\overline{u'^2}$  and  $\overline{v'^2}$ ) components are  
393 calculated as the moving variance in a 10s window centered at the measurement time. The  $w$  data is  
394 confined to an absolute aircraft roll angle of less than  $5^\circ$  (Cooper et al., 2016).

395 As shown in Figure 5, the vertical wind variances (Fig. 5b) in ACE-ENA winter (layer-mean of  $0.244$   
396  $\text{m}^2 \text{s}^{-2}$ ) are generally higher than those in summer ( $0.153 \text{m}^2 \text{s}^{-2}$ ) and SOCRATES ( $0.147 \text{m}^2 \text{s}^{-2}$ ), while  
397 the horizontal wind variances are comparable between ACE-ENA winter and summer but much higher  
398 than the SOCRATES, resulting in higher TKE during ACE-ENA. Near the cloud top, turbulence  
399 effectively enhances coalescence between the larger cloud droplets, primarily by increasing the relative  
400 velocities between droplets (Magaritz-Ronen et al., 2016; Ghate and Cadeddu, 2019), and this is  
401 especially true for the vertical component of TKE. Note that the values of the vertical turbulence are  
402 generally within the ranges of previous studies (Atlas et al., 2020; Ghate et al., 2021). Hence, the stronger  
403 drizzle formation in the ACE-ENA winter clouds can be attributed to the higher  $w'^2$  (Fig. 5b) near cloud  
404 top (which also explains the stronger entrainment in winter), while the similar  $w'^2$  correspond to the  
405 comparable  $N_d$  between the ACE-ENA summer and SOCRATES. The presence of turbulence  
406 throughout the cloud layer induces differential motions among the cloud droplets, increasing the  
407 likelihood of drizzle collecting smaller droplets and the droplets coalescing (Brost et al., 1982; Feingold



408 et al., 1996). As a result, the drizzle DSD is sufficiently broadened, and the  $D_{mmd}$  is enlarged toward the  
409 cloud base.

410 It is noteworthy that the  $D_{mmd}$  in the lower-half region of the ACE-ENA winter clouds experienced  
411 rapid growth from  $\sim 80 \mu\text{m}$  to  $\sim 105 \mu\text{m}$  (Fig. 3e), and this increment of  $\sim 25 \mu\text{m}$  contributed to most of  
412 the  $D_{mmd}$  growth from cloud top to cloud base ( $33.5 \mu\text{m}$ ). Such phenomena may potentially owe to the  
413 much stronger  $w'^2$  in the low half cloud (Fig. 5b), where the sufficient updraft can slow down the descent  
414 of drizzle drops, thus recirculating them and elongating the drizzle residence time in the lower part of the  
415 cloud, effectively enhancing the collision-coalescence growth (Feingold et al., 1996; Magaritz et al.,  
416 2009). In terms of the horizontal turbulence components, the  $u'^2$  and  $v'^2$  can play a role in mixing the  
417 ambient air masses and contribute to the broadening of DSD (Wu et al., 2017). However, the vertical  
418 turbulence is generally more directly influential to the drizzle formation and evolution (Brost et al., 1982;  
419 Nicholls, 1984; Pinsky and Khain, 1997; Ghate et al., 2021).

420

#### 421 **4 Aerosol-cloud-precipitation interactions (ACPIs)**

##### 422 **4.1 Cloud microphysical responses on aerosols**

423 The impacts of different aerosol loadings onto the cloud microphysical properties can be assessed  
424 by the aerosol-cloud interaction (ACI) indices, which can be quantified as:

$$425 \quad ACI_N = \frac{\partial \ln(N_c)}{\partial \ln(N_{CCN,0.35\%})}, \quad (8)$$

426 and

$$427 \quad ACI_r = -\frac{\partial \ln(r_c)}{\partial \ln(N_{CCN,0.35\%})}, \quad (9)$$

428 which emphasizes the cloud microphysical responses to CCN via the relative logarithmic change of  $N_c$   
429 and  $r_c$  to the change in  $N_{CCN,0.35\%}$  (Feingold et al., 2003; McComiskey et al., 2009). Physically, the ACI  
430 process involves aerosols intruding into the cloud layer, activating as cloud droplets, and subsequently  
431 altering cloud DSD and dispersion (Zheng et al., 2022a&b) under various water vapor availabilities.



432 Therefore, the cloud microphysical responses within the lower region of the cloud are assessed, which is  
433 the first stage in which the sub-cloud CCN can directly interact with the cloud droplets. Furthermore, the  
434 similarity in the mean  $LWC_c$  (as shown in Fig. 3c) provides comparable liquid water between three IOPs  
435 for the assessment of newly generated cloud embryos from activated CCN because the  $ACI_r$  is normally  
436 assessed under a fixed liquid water (Zheng et al., 2020).

437 Considering all the cases from three IOPs with available CCN measurements (some cases without  
438 CCN measurements during SOCRATES), the  $N_c$  and  $r_c$  at the lower cloud ( $z_l < 0.2$ ) are plotted against  
439 the sub-cloud  $N_{CCN,0.35\%}$  in Figure 6, and the ACI indices are calculated as  $ACI_{N,CB}$  and  $ACI_{r,CB}$  (CB  
440 denoting the assessment near the cloud base). Note that the availability of valid sub-cloud measurements  
441 inevitably limit the sample size, especially for SOCRATES, as shown in Table S2. As shown in Figure  
442 6a, the  $ACI_{N,CB}$  for the ACE-ENA wintertime (0.748) is higher than the summertime (0.617), indicating  
443 that  $N_c$  is more sensitive to the sub-cloud  $N_{CCN,0.35\%}$ . In other words, aerosols intruding into the cloud  
444 layer are easily activated to become cloud droplets, which agrees with the previous assessment by J.  
445 Wang et al. (2022) on the seasonal dependency of the relationship between  $N_c$  and aerosols. The  $N_c$   
446 sensitivity for the SOCRATES cloud (0.692) lies between the two ACE-ENA IOPs. The  $ACI_{N,CB}$  values  
447 from three IOPs are generally higher than the  $ACI_N$  values from the layer-mean  $N_c$  against the sub-cloud  
448  $N_{CCN,0.35\%}$  (not shown). Previous studies have shown that the enhanced vertical turbulence (updraft  
449 velocity) can effectively facilitate CCN replenishment into the cloud layer (Zheng et al., 2022a&b) and  
450 increase the actual in-cloud supersaturation (Brunke et al., 2022), thus leading to a more efficient cloud  
451 droplet formation, enhancing the  $ACI_{N,CB}$ . Furthermore, more coarse mode aerosols during ACE-ENA  
452 winter are also favorable to the activation efficiency (Dusek et al., 2006).

453 As for the  $r_c$  responses to CCN (Fig. 6b), the typical Twomey effect, where more CCN compete  
454 against available water vapor and result in smaller cloud droplets, is evidenced by different cloud  
455 susceptibility between the three IOPs. The SOCRATES features a higher  $ACI_{r,CB}$  (0.311), suggesting



456 that an increase in  $N_{CCN,0.35\%}$  can result in a significant decrease in  $r_c$ , compared to ACE-ENA summer  
457 (0.206) and winter (0.263). Although the absolute range of variation for  $r_c$  during SOCRATES is smaller,  
458 the slope is much deeper (Fig. 6b). Recall that the sub-cloud  $N_{CCN,0.35\%}$  during SOCRATES is generally  
459 higher and is constituted by more small-sized aerosols (as indicated in Fig. 2b). Consequently, after  
460 activation, the lower part of the cloud exhibits a higher number of smaller cloud droplets, as shown in  
461 Fig. 4d, even under the relatively less  $N_{CCN,0.35\%}$  condition for SOCRATES. Therefore, as more CCN  
462 intrudes into the cloud, the competition for water vapor among newly-activated cloud droplets becomes  
463 more pronounced, given similar water availability. In contrast, the presence of larger cloud droplets near  
464 the cloud base, whether activated from coarse-mode aerosols or remaining as residuals from cloud  
465 coalescence, would elevate the  $r_c$  especially under the relatively more CCN condition, hence inevitably  
466 dampening the  $ACI_{r, CB}$  during ACE-ENA. However, a more comprehensive investigation into the cloud  
467 microphysical responses to CCN intrusions under various water supply conditions will require additional  
468 aircraft cases from more field campaigns. Note that the  $ACI_{r, CB}$  values in Figure 6b are also larger than  
469 the results from the layer-mean  $r_c$  against sub-cloud  $N_{CCN,0.35\%}$ , since the layer-mean microphysics is  
470 more subject to the cloud droplet evolution processes such as condensational growth and collision-  
471 coalescence. The ACI indices from three IOPs are in the ACI range of the previous studies in MBL  
472 clouds (Twohy et al., 2005; Lu et al., 2009; Diamond et al., 2018) using aircraft in-situ measurements.

473 To investigate the ACI indices at the upper level of the cloud, the  $N_c$  and  $r_c$  at the upper cloud ( $z_i >$   
474 0.8) are plotted against the above-cloud  $N_{CCN,0.35\%}$  in Figure S5, and the ACI indices are calculated as  
475  $ACI_{N, CT}$  and  $ACI_{r, CT}$  (denoting the assessments near the cloud top). Compared to the  $ACI_{N, CB}$  and  
476  $ACI_{r, CB}$ , the  $ACI_{N, CT}$  and  $ACI_{r, CT}$  are much weaker, especially for  $ACI_{r, CT}$ . These weaker relationships  
477 support the notion that though the aerosols entrained into the upper-cloud region can affect the cloud  
478 microphysics to a certain degree, the effects are less pronounced than those from the sub-cloud aerosols



479 (Diamond et al., 2018, Wang et al., 2020) because the MBL cloud  $N_c$  and  $r_c$  variations are dominated by  
480 the condensational growth process and the collision-coalescence process near the cloud top.

481

## 482 **4.2 Precipitation susceptibility**

483 The precipitation susceptibility relies on the assessment of relative responses in the precipitation  
484 rate to the change in  $N_c$  (Sorooshian et al., 2009), which is defined as:

$$485 S_o = -\frac{\partial \ln(R_{CB})}{\partial \ln(N_c)}, \quad (10)$$

486 where the  $R_{CB}$  is the cloud base precipitation rate calculated in section 2 (equation 5). By incorporating  
487 all the cloud cases, including both precipitating and non-precipitating clouds (the  $R_{CB}$  can also be  
488 calculated based on the drizzle DSD near the cloud base), the  $S_o$  accounts for the impact of cloud droplets  
489 on the potential precipitation ability of the cloud (Terai et al., 2012).

490 As shown in Figure 7a, the  $R_{CB}$  values generally have a negative correlation with increased layer-  
491 mean  $N_c$  with the  $S_o$  values of 0.979, 1.229 and 1.638, respectively, for SOCRATES, ACE-ENA summer  
492 and winter. Note that the  $R_{CB}$  for the ACE-ENA winter is more susceptible to the layer-mean  $N_c$  than the  
493 ACE-ENA summer and SOCRATES, which can be partially attributed to the existence of more large  
494 drizzle drops (as shown in Fig. 4d) near the cloud base. As previously discussed, these large drizzle drops  
495 are induced by the turbulence-enhanced in-cloud collision-coalescence and the drizzle-recirculating  
496 processes, especially under low  $N_c$  conditions, hence increasing the  $S_o$  values. Comparing the  
497 seasonality during ACE-ENA, more cases with large observed  $R_{CB}$  during the winter season are  
498 consistent with J. Wang et al. (2022). The relatively narrower drizzle DSD in SOCRATES may further  
499 diminish the sensitivity of  $R_{CB}$  to  $N_c$ . Note that the derived  $S_o$  values in this study are generally higher  
500 (or close to the upper end) compared to previous studies (Lu et al., 2009; Duong et al., 2011; Terai et al.,  
501 2012; Jung et al., 2016), which is possibly due to decreasing  $S_o$  within the thicker cloud (Terai et al.,



502 2012). The mean cloud thicknesses of the ACE-ENA summer (368.7 m), winter (400.8 m) and  
503 SOCRATES (487.4 m) are inversely proportional to their  $S_o$  values.

504 In addition, it is well known that the  $R_{CB}$  can be parameterized or predicted via an approximate  
505 relation with  $N_c$  and cloud thickness ( $H_c$ ), which is usually parameterized in the form of  $R_{CB} \propto c H_c^3 N_c^{-1}$   
506 (Lu et al., 2009). Following the same method, we derive the relationships from three IOPs in Figure 7b,  
507 where the  $R_{CB}$  are positively (negatively) proportional to the  $H_c$  ( $N_c$ ), with the exponential parameters in  
508 the range of the typical values in the MBL clouds (Comstock et al., 2004; vanZanten et al., 2005; Lu et  
509 al., 2009). The statistical  $R^2$  values of  $R_{CB}$  against  $H_c$  ( $N_c$ ) are 0.696 (0.177), 0.419 (0.212) and 0.165  
510 (0.295), for the ACE-ENA summer, winter and SOCRATES, respectively, suggesting that the  $R_{CB}$  in  
511 ACE-ENA clouds may be more determined by  $H_c$ , while the  $R_{CB}$  in SOCRATES cloud are more related  
512 to  $N_c$ . Note that the relationship for SOCRATES in this study reveals a similar  $R_{CB}$  dependence on  $N_c$   
513 but a smaller dependence on the cloud thickness than the study by Kang et al. (2023), who concluded a  
514 relationship of  $R_{CB} = 1.73e - 10 H_c^{3.6} N_a^{-1}$ , based on the rain rate retrieved from radar and lidar  
515 measurements and the aerosol concentration also from the SOCRATES. The discrepancies are possibly  
516 due to the different sample selections and different methods in the  $R_{CB}$  calculation.

517

#### 518 **4.3 Drizzle impacts on sub-cloud CCN and implication to ACI**

519 Multiple studies on the MBL clouds have concluded that the in-cloud drizzle formation and  
520 evolution processes can effectively impact the sub-cloud CCN budgets via the coalescence-scavenging  
521 effect (Wood, 2006; Wood et al., 2012; Diamond et al., 2018; Zheng et al., 2022b; Zhang et al., 2023).  
522 Drizzle drops are formed and grow via the collision-coalescence process by collecting cloud droplets and  
523 small drizzle drops, resulting in the consumption of CCN (the precursor of cloud droplet), but in the  
524 meantime, the in-cloud  $N_c$  can be continuously buffered by the sub-cloud CCN replenishment. Although  
525 the sub-cloud aerosols (especially in large size) would be added if the drizzle fell and evaporated outside



526 the cloud, the increment cannot compensate for the loss. Therefore, the net result of the whole process is  
527 usually presented as the depletion of sub-cloud CCN residuals, and such drizzle modulation on the CCN  
528 budget could be substantial in moderate-to-light drizzles or even non-precipitating clouds, depending on  
529 the collision-coalescence efficiency (Feingold et al., 1996; Wood, 2006; Kang et al., 2022).

530 The CCN loss rate due to the coalescence-scavenging effect can be calculated as:

$$531 \quad L_{CCN} = -\frac{K H_c}{H_{mix}} * N_c * R_{CB}, \quad (11)$$

532 where the constant K ( $2.25 \text{ m}^2 \text{ kg}^{-1}$ ) denotes the drizzle collection efficiency (Wood et al., 2006; Diamond  
533 et al., 2018).  $H_c$  is cloud thickness, and  $H_{mix}$  is the thickness of the mixed layer to ensure the change in  
534 the cloud layer can be sufficiently conveyed throughout the layer. The calculated CCN loss rate for  
535 individual cases is listed in Table S2. Considering all cloud (precipitating cloud) scenarios, the mean  
536 CCN loss rates are  $-7.69 \pm 13.96 \text{ cm}^{-3}$  ( $-10.45 \pm 15.56 \text{ cm}^{-3}$ ),  $-6.29 \pm 11.65 \text{ cm}^{-3}$  ( $12.11 \pm 14.64 \text{ cm}^{-3}$ ), and -  
537  $4.94 \pm 7.96 \text{ cm}^{-3}$  ( $-5.58 \pm 8.43 \text{ cm}^{-3}$ ) for ACE-ENA summer, winter and SOCRATES, respectively.  
538 Indicating the ACE-ENA clouds suffer more substantial sub-cloud CCN loss than the SOCRATES,  
539 especially for the wintertime precipitating clouds. Recall that the assessment of  $ACI_{r,CB}$  relies on the  
540 relative changes of  $r_c$  and  $N_{CCN}$ , while the different  $L_{CCN}$  for individual cases can result in the shrinking  
541 of the  $N_{CCN}$  variation ranges (imagine the abundant CCN are depleted by the coalescence scavenging).  
542 In other words, the given change in  $r_c$  corresponds to a narrowed change in  $N_{CCN}$ , hence mathematically  
543 presented as an enlarged  $ACI_{r,CB}$ . Hence, the coalescence-scavenging effect can not only deplete the sub-  
544 cloud CCN, but also quantitatively amplify the assessment of cloud microphysics susceptibilities  
545 (Feingold et al., 1999; Duong et al., 2011; Jung et al., 2016; Zheng et al., 2022b). In order to examine  
546 the potential impact of the aforementioned processes on the  $ACI$  assessment, a sensitivity analysis is  
547 conducted by simply retrospectively the sub-cloud  $N_{CCN0.35\%}$  according to their  $L_{CCN}$  and recalculate the  
548  $ACI_{r,CB}$ .



549 As shown in Figure 8, the  $ACI_{r,CB}$  values tend to decrease with the retrospective time, which  
550 indicates the retrospective CCN variation range is enlarged and counteracting the coalescence-  
551 scavenging amplification. The detailed illustration of the different  $ACI_{r,CB}$  calculated from the scattered  
552  $r_c$  and sub-cloud  $N_{CCN0.35\%}$  is shown in Figure S6. Note that the  $ACI_{r,CB}$  decreasing rates for the  
553 precipitating clouds (Fig. 8b) are not as strong as for all clouds because the non-precipitating clouds have  
554 smaller  $L_{CCN}$  largely due to weaker collision-coalescence. Hence, the time retrospected might quickly  
555 exceed the actual time scale of processing of cloud droplets. In other words, the time needed to store the  
556 sub-cloud CCN to the budget before cloud existence is shorter. Therefore, the retrospective of the sub-  
557 cloud CCN budget will yield an alternative assessment of ACI, assuming that the drizzle processes have  
558 not yet significantly impacted the sub-cloud CCN budget, especially for the assessment under the  
559 precipitating clouds. However, examining the exact precipitating timing is challenging since the aircraft  
560 provides a snapshot of the cloud and aerosol information. Thus, this retrospective study only provides a  
561 possible direction, and the result should be interpreted with caution.

562

## 563 **5. Summary and Conclusions**

564 Based on the aircraft in-situ measurements during ACE-ENA and SOCRATES, the vertical  
565 distributions and the evolutions of the aerosol, cloud, and drizzle properties are investigated under the  
566 cloud-topped MBL environments. The aerosols and CCN from SOCRATES are the highest among the  
567 three IOPs, followed by ACE-ENA summer and winter in descending order in both above- and sub-cloud  
568 regimes. The differences can be attributed to the aerosol sources in both regions, where the SOCRATES  
569 represents the pristine natural environment enriched by aerosols from marine biological productivity and  
570 without the contamination of anthropogenic aerosols, while the ACE-ENA features the aerosols from  
571 varied sources, including maritime and continental emissions, with distinct seasonal variations.  
572 Examining the aerosol size distributions in sub-cloud versus above-cloud regimes manifests the





573 significant influence of cloud processing on aerosols. Physical processing like in-cloud Brownian capture  
574 can reduce Aitken mode aerosols, while the chemical processes transform Aitken mode aerosols to larger  
575 sizes, moving them toward the accumulation mode. In addition, the in-cloud coalescence processes shift  
576 sub-cloud aerosol residuals to larger sizes, explaining the observed increase in the tail-end of the aerosol  
577 distribution for all IOPs.

578 As for the cloud and drizzle properties, the SOCRATES clouds feature more and smaller cloud  
579 droplets than the ACE-ENA summertime and wintertime clouds, with the  $r_c$  growths, from cloud base to  
580 top, being  $4.03 \mu\text{m}$ ,  $4.78 \mu\text{m}$ , and  $5.85 \mu\text{m}$  for SOCRATES, ACE-ENA summer, and winter, respectively.  
581 The cloud-top entrainment mixing is evidenced in the observed decline of both  $N_c$  and  $LWC_c$  near the  
582 cloud top. The mean cloud-top entrainment rates ( $w_e$ ) as a function of cloud top virtual potential  
583 temperature and vertical velocity are  $0.570 \pm 0.834 \text{ cm s}^{-1}$ ,  $0.581 \pm 0.560 \text{ cm s}^{-1}$ , and  $0.960 \pm 1.127 \text{ cm s}^{-1}$   
584 for SOCRATES, ACE-ENA summer and winter, respectively. The strongest  $w_e$  during ACE-ENA  
585 winter is owing to weaker cloud-top inversions and stronger near-cloud-top turbulence. For drizzle  
586 vertical distribution,  $N_d$  from the three IOPs all exhibit decreases from cloud top to cloud base, while  
587  $D_{\text{modal}}$  are in opposite directions with a maximum at the cloud base. The ACE-ENA wintertime clouds  
588 feature more prominent drizzle formation and evolution owing to the strong in-cloud TKE, especially  
589 the strongest vertical turbulence in the lower half of the cloud layer, which substantially enhances the  
590 collision-coalescence process, compared to the other two IOPs.

591 The cloud sub-adiabaticity  $f_{ad}$  values are  $0.681 \pm 0.083$ ,  $0.476 \pm 0.106$ , and  $0.447 \pm 0.100$  for  
592 SOCRATES, ACE-ENA summer and winter, respectively. While the satellite retrievals of droplet  
593 number concentration heavily rely on the adiabatic cloud assumption and are usually given as a constant  
594 of  $f_{ad} = 0.8$ . Hence, the in-situ observational evidence of the variability of MBL cloud and drizzle  
595 microphysical properties over different regions shed light on the further understanding of the satellite



596 retrievals, particularly the satellite-based aerosol-cloud interaction assessment (Painemal and Zuidema,  
597 2011; Grosvenor et al., 2018; Painemal et al., 2021).

598 Notably, the sensitivity of cloud base precipitation rate ( $R_{CB}$ ) to  $N_c$  is more pronounced for the  
599 ACE-ENA during both winter (with  $S_o = 1.638$ ) and summer (1.229) compared to the SOCRATES ( $S_o$   
600 = 0.979). This is partly due to the much higher  $R_{CB}$  induced by larger drizzle drops near the cloud base  
601 for ACE-ENA, a result of turbulence-driven in-cloud droplet interactions, especially under low  $N_c$   
602 condition. Furthermore,  $R_{CB}$  can be approximated by a relationship involving  $N_c$  and  $H_c$ , as suggested in  
603 prior research. The relationships established in this study indicate that ACE-ENA clouds, are largely  
604 determined by  $H_c$ , while SOCRATES clouds are more influenced by the  $N_c$ .

605 The investigations of the ACI via the  $ACI_{N,CB}$  and  $ACI_{r,CB}$  indices reveal that during the ACE-  
606 ENA wintertime,  $N_c$  is more sensitive to changes in  $N_{CCN0.35\%}$ , indicating aerosols more readily activate  
607 to become cloud droplets. One influencing factor is the strong vertical turbulence, which speeds up the  
608 infusion of CCN into the cloud layer, thus aiding droplet formation. Furthermore, the presence of larger  
609 aerosols during ACE-ENA winter enhances the droplet activation process. The SOCRATES IOP  
610 highlights a higher  $ACI_{r,CB}$ , indicating a pronounced decrease in  $r_c$  with increasing  $N_{CCN0.35\%}$ . While the  
611  $ACI_{r,CB}$  in ACE-ENA is dampened by the presence of more larger cloud droplets near the cloud base,  
612 particularly under relatively higher  $N_{CCN0.35\%}$ . Note that the ACI indices from this study lie in the higher  
613 end of the ACI ranges estimated via remote sensing (McComiskey et al., 2009; Dong et al., 2015; Zheng  
614 et al., 2022a) because the aircraft assessment provides more connected circumstances between the  
615 aerosols and cloud layer. Arguably, the assessment of  $N_c$  responses to  $N_{CCN0.35\%}$  would inevitably be  
616 affected by the collision-coalescence process near the cloud base, where simultaneously, the CCN  
617 replenishment buffers the  $N_c$  and the collision-coalescence process depletes  $N_c$ . Hence, finding a layer  
618 where these two effects maintain a dynamic balance in  $N_c$  might aid in a more accurate assessment and



619 more fundamental understanding of the ACI, which might be revealed by the LES or parcel model  
620 simulations.

621 Additionally, the in-cloud drizzle formation and evolution processes significantly influence the  
622 sub-cloud CCN budgets via the coalescence-scavenging effect, which can potentially exaggerate the  
623 assessment of cloud microphysics susceptibilities. Based on the CCN loss rate ( $L_{CCN}$ ) from ACE-ENA  
624 and SOCRATES, a sensitivity analysis is performed focusing on retrospectively adjusting the sub-cloud  
625 CCN according to their  $L_{CCN}$ . Results showed that this adjustment led to a decreased  $ACI_{r,CB}$ ,  
626 highlighting the significance of the coalescence-scavenging process on the ACI assessment. However,  
627 due to the fact that aircraft only provide a snapshot of the clouds and aerosol information, determining  
628 the precise drizzle timing for the individual cloud is challenging. Hence, findings from this retrospective  
629 approach provide only a direction or theory, and should be taken cautiously. Nevertheless, pursuing  
630 further modeling experiments on this matter may be worthwhile. For example, the exact drizzling time  
631 could be pinpointed within a model using an Eulerian framework or traced using a Lagrangian framework.  
632 Nevertheless, the CCN adjustment could more accurately reflect the true characteristics of the cloud and  
633 the MBL CCN budget, potentially aiding in a more precise assessment of ACI. Therefore, future works  
634 would focus on the model simulation on the MBL clouds from ACE-ENA and SOCRATES and further  
635 assess the modeled ACI under the observational constraints, as well as the continuous development of  
636 the warm rain microphysical parameterizations, in order to aid in the better represent the MBL clouds in  
637 multiple regions.

638

639

640 *Data availability.* The ACE-ENA field campaign data can be accessed from the Department of Energy  
641 Atmospheric Radiation Measurement data archive ([https://iop.archive.arm.gov/arm-iop-](https://iop.archive.arm.gov/arm-iop-file/2017/ena/accena/)  
642 [file/2017/ena/accena/](https://iop.archive.arm.gov/arm-iop-file/2017/ena/accena/)). The SOCRATES field campaign data are publicly archived on the National



643 Center for Atmospheric Research (NCAR) Earth Observing Laboratory  
644 ([https://data.eol.ucar.edu/master\\_lists/generated/socrates/](https://data.eol.ucar.edu/master_lists/generated/socrates/)).

645

646 *Author contributions.* The original idea of this study is discussed by XZ, XD, and BX. XZ performed the  
647 analyses and wrote the manuscript. XZ, XD, BX, TL, and YW participated in further scientific  
648 discussions and provided substantial comments and edits on the paper.

649

650 *Competing interests.* At least one of the (co-)authors is a member of the editorial board of Atmospheric  
651 Chemistry and Physics.

652

653 *Acknowledgments.* This work was supported by the NSF grants AGS-2031750/2031751/20211752 at the  
654 University of Arizona, Texas A&M University and Stanford University, respectively. The authors  
655 sincerely thank the investigators and mentors from the ACE-ENA and SOCRATES field campaigns for  
656 making the data publicly available.

657

## 658 **References.**

659 Albrecht B. A.: Aerosols, Cloud Microphysics, and Fractional Cloudiness, *Science*, 245, 1227-1230,  
660 10.1126/science.245.4923.1227, 1989

661 Albrecht, B. A., Bretherton, C. S., Johnson, D., Scubert, W. H., and Frisch, A. S.: The Atlantic  
662 Stratocumulus Transition Experiment—ASTEX, *B. Am. Meteorol. Soc.*, 76, 889-904,  
663 10.1175/1520-0477(1995)076<0889:Taste>2.0.Co;2, 1995.

664 Albrecht, B., Fang, M., and Ghate, V.: Exploring Stratocumulus Cloud-Top Entrainment Processes and  
665 Parameterizations by Using Doppler Cloud Radar Observations, *J. Atmos. Sci.*, 73, 729-742,  
666 10.1175/JAS-D-15-0147.1, 2016.



- 667 Atlas, R. L., Bretherton, C. S., Blossey, P. N., Gettelman, A., Bardeen, C., Lin, P., and Ming, Y.: How  
668 Well Do Large-Eddy Simulations and Global Climate Models Represent Observed Boundary Layer  
669 Structures and Low Clouds Over the Summertime Southern Ocean?, *Journal of Advances in*  
670 *Modeling Earth Systems*, 12, e2020MS002205, <https://doi.org/10.1029/2020MS002205>, 2020.
- 671 Atlas, R., Mohrmann, J., Finlon, J., Lu, J., Hsiao, I., Wood, R., and Diao, M.: The University of  
672 Washington Ice–Liquid Discriminator (UWILD) improves single-particle phase classifications of  
673 hydrometeors within Southern Ocean clouds using machine learning, *Atmos. Meas. Tech.*, 14,  
674 7079-7101, [10.5194/amt-14-7079-2021](https://doi.org/10.5194/amt-14-7079-2021), 2021.
- 675 Baumgardner, D. and Korolev, A.: Airspeed Corrections for Optical Array Probe Sample Volumes, *J.*  
676 *Atmos. Ocean. Tech.*, 14, 1224-1229, [https://doi.org/10.1175/1520-](https://doi.org/10.1175/1520-0426(1997)014<1224:ACFOAP>2.0.CO;2)  
677 [0426\(1997\)014<1224:ACFOAP>2.0.CO;2](https://doi.org/10.1175/1520-0426(1997)014<1224:ACFOAP>2.0.CO;2), 1997.
- 678 Baumgardner, D., Abel, S. J., Axisa, D., Cotton, R., Crosier, J., Field, P., Gurganus, C., Heymsfield, A.,  
679 Korolev, A., Krämer, M., Lawson, P., McFarquhar, G., Ulanowski, Z., and Um, J.: Cloud Ice  
680 Properties: In Situ Measurement Challenges, *Meteor. Monogr.*, 58, 9.1-9.23,  
681 <https://doi.org/10.1175/AMSMONOGRAPHS-D-16-0011.1>, 2017.
- 682 Braun, R. A., Dadashazar, H., MacDonald, A. B., Crosbie, E., Jonsson, H. H., Woods, R. K., Flagan, R.  
683 C., Seinfeld, J. H., and Sorooshian, A.: Cloud Adiabaticity and Its Relationship to Marine  
684 Stratocumulus Characteristics Over the Northeast Pacific Ocean, *J. Geophys. Res.-Atmos.*, 123,  
685 13790 - 13806, [10.1029/2018jd029287](https://doi.org/10.1029/2018jd029287), 2018.
- 686 Brost, R. A., Wyngaard, J. C., and Lenschow, D. H.: Marine Stratocumulus Layers. Part II: Turbulence  
687 Budgets, *J. Atmos. Sci.*, 39, 818-836, [10.1175/1520-0469\(1982\)039<0818:MSLPIT>2.0.CO;2](https://doi.org/10.1175/1520-0469(1982)039<0818:MSLPIT>2.0.CO;2),  
688 1982.
- 689 Brunke, M. A., Cutler, L., Urzua, R. D., Corral, A. F., Crosbie, E., Hair, J., Hostetler, C., Kirschler, S.,  
690 Larson, V., Li, X.-Y., Ma, P.-L., Minke, A., Moore, R., Robinson, C. E., Scarino, A. J., Schlosser,  
691 J., Shook, M., Sorooshian, A., Lee Thornhill, K., Voigt, C., Wan, H., Wang, H., Winstead, E., Zeng,



- 692 X., Zhang, S., and Ziemba, L. D.: Aircraft Observations of Turbulence in Cloudy and Cloud-Free  
693 Boundary Layers Over the Western North Atlantic Ocean From ACTIVATE and Implications for  
694 the Earth System Model Evaluation and Development, *J. Geophys. Res.-Atmos.*, 127,  
695 e2022JD036480, <https://doi.org/10.1029/2022JD036480>, 2022.
- 696 Chen, S., Yau, M. K., and Bartello, P.: Turbulence Effects of Collision Efficiency and Broadening of  
697 Droplet Size Distribution in Cumulus Clouds, *J. Atmos. Sci.*, 75, 203-217,  
698 <https://doi.org/10.1175/JAS-D-17-0123.1>, 2018.
- 699 Chen, Y. C., Xue, L., Lebo, Z. J., Wang, H., Rasmussen, R. M., and Seinfeld, J. H.: A comprehensive  
700 numerical study of aerosol-cloud-precipitation interactions in marine stratocumulus, *Atmos. Chem.*  
701 *Phys.*, 11, 9749-9769, 10.5194/acp-11-9749-2011, 2011.
- 702 Comstock, K. K., Wood, R., Yuter, S. E., and Bretherton, C. S.: Reflectivity and rain rate in and below  
703 drizzling stratocumulus, *Q. J. R. Meteor. Soc.*, 130, 2891-2918, <https://doi.org/10.1256/qj.03.187>,  
704 2004.
- 705 Cooper, W. A., Friesen, R. B., Hayman, M., Jensen, J., Lenschow, D. H., Romashkin, P., Schanot, A., Spuler, S.,  
706 Stith, J., and Wolff, C.: Characterization of Uncertainty in Measurements of Wind from the NSF/NCAR  
707 Gulfstream V Research Aircraft (No. NCAR/TN-528+STR), NCAR Technical Notes,  
708 doi:10.5065/D60G3HJ8, 2016.
- 709 Covert, D. S., Kapustin, V. N., Bates, T. S., and Quinn, P. K.: Physical properties of marine boundary  
710 layer aerosol particles of the mid-Pacific in relation to sources and meteorological transport, *J.*  
711 *Geophys. Res.-Atmos.*, 101, 6919-6930, <https://doi.org/10.1029/95JD03068>, 1996.
- 712 D'Alessandro, J. J., McFarquhar, G. M., Wu, W., Stith, J. L., Jensen, J. B., and Rauber, R. M.:  
713 Characterizing the Occurrence and Spatial Heterogeneity of Liquid, Ice, and Mixed Phase Low-  
714 Level Clouds Over the Southern Ocean Using in Situ Observations Acquired During SOCRATES,  
715 *J. Geophys. Res.-Atmos.*, 126, e2020JD034482, <https://doi.org/10.1029/2020JD034482>, 2021.



- 716 Desai, N., Liu, Y., Glienke, S., Shaw, R. A., Lu, C., Wang, J., and Gao, S.: Vertical Variation of Turbulent  
717 Entrainment Mixing Processes in Marine Stratocumulus Clouds Using High-Resolution Digital  
718 Holography, *J. Geophys. Res.-Atmos.*, 126, e2020JD033527,  
719 <https://doi.org/10.1029/2020JD033527>, 2021.
- 720 Dong, X., Schwantes, A. C., Xi, B., and Wu, P.: Investigation of the marine boundary layer cloud and  
721 CCN properties under coupled and decoupled conditions over the Azores, *J. Geophys. Res.-Atmos.*,  
722 120, 6179-6191, <https://doi.org/10.1002/2014JD022939>, 2015.
- 723 Dong, X., X. Zheng, B. Xi, and S. Xie (2023), A Climatology of Midlatitude Maritime Cloud Fraction and  
724 Radiative Effect Derived from the ARM ENA Ground-Based Observations, *J. Climate*, 36(2), 531-546,  
725 doi:10.1175/JCLI-D-22-0290.1.
- 726 Duong, H. T., Sorooshian, A., and Feingold, G.: Investigating potential biases in observed and modeled  
727 metrics of aerosol-cloud-precipitation interactions, *Atmos. Chem. Phys.*, 11, 4027-4037,  
728 10.5194/acp-11-4027-2011, 2011.
- 729 Feingold, G., Frisch, A. S., Stevens, B., and Cotton, W. R.: On the relationship among cloud turbulence,  
730 droplet formation and drizzle as viewed by Doppler radar, microwave radiometer and lidar, *J.*  
731 *Geophys. Res.-Atmos.*, 104, 22195-22203, <https://doi.org/10.1029/1999JD900482>, 1999.
- 732 Feingold, G., Kreidenweis, S. M., Stevens, B., and Cotton, W. R.: Numerical simulations of  
733 stratocumulus processing of cloud condensation nuclei through collision-coalescence, *J. Geophys.*  
734 *Res.-Atmos.*, 101, 21391-21402, <https://doi.org/10.1029/96JD01552>, 1996.
- 735 Gao, S., Lu, C., Liu, Y., Mei, F., Wang, J., Zhu, L., and Yan, S.: Contrasting Scale Dependence of  
736 Entrainment-Mixing Mechanisms in Stratocumulus Clouds, *Geophys. Res. Lett.*, 47,  
737 e2020GL086970, <https://doi.org/10.1029/2020GL086970>, 2020.
- 738 Ghate, V. P. and Cadetdu, M. P.: Drizzle and Turbulence Below Closed Cellular Marine Stratocumulus  
739 Clouds, *J. Geophys. Res.-Atmos.*, 124, 5724-5737, <https://doi.org/10.1029/2018JD030141>, 2019.



- 740 Ghate, V. P., Cadeddu, M. P., Zheng, X., and O'Connor, E.: Turbulence in the Marine Boundary Layer  
741 and Air Motions below Stratocumulus Clouds at the ARM Eastern North Atlantic Site, *J. Appl.*  
742 *Meteorol. Clim.*, 60, 1495-1510, 10.1175/JAMC-D-21-0087.1, 2021.
- 743 Grabowski, W. W. and Wang, L.-P.: Growth of Cloud Droplets in a Turbulent Environment, *Annual*  
744 *Review of Fluid Mechanics*, 45, 293-324, 10.1146/annurev-fluid-011212-140750, 2013.
- 745 Grosvenor, D. P., Sourdeval, O., Zuidema, P., Ackerman, A., Alexandrov, M. D., Bennartz, R., Boers,  
746 R., Cairns, B., Chiu, J. C., Christensen, M., Deneke, H., Diamond, M., Feingold, G., Fridlind, A.,  
747 Hünerbein, A., Knist, C., Kollias, P., Marshak, A., McCoy, D., Merk, D., Painemal, D., Rausch, J.,  
748 Rosenfeld, D., Russchenberg, H., Seifert, P., Sinclair, K., Stier, P., van Dierenhoven, B., Wendisch,  
749 M., Werner, F., Wood, R., Zhang, Z., and Quaas, J.: Remote Sensing of Droplet Number  
750 Concentration in Warm Clouds: A Review of the Current State of Knowledge and Perspectives,  
751 *Reviews of Geophysics*, 56, 409-453, <https://doi.org/10.1029/2017RG000593>, 2018.
- 752 Hill, A. A., Feingold, G., and Jiang, H.: The Influence of Entrainment and Mixing Assumption on  
753 Aerosol-Cloud Interactions in Marine Stratocumulus, *J. Atmos. Sci.*, 66, 1450-1464,  
754 10.1175/2008JAS2909.1, 2009.
- 755 Hinds, W.C.: *Aerosol Technology, Properties, Behaviour, and Measurement of Airborne Particles*. John Wiley &  
756 Sons Inc., New York., 1999.
- 757 Jung, E., Albrecht, B. A., Sorooshian, A., Zuidema, P., and Jonsson, H. H.: Precipitation susceptibility  
758 in marine stratocumulus and shallow cumulus from airborne measurements, *Atmos. Chem. Phys.*,  
759 16, 11395-11413, 10.5194/acp-16-11395-2016, 2016.
- 760 Kang, L., Marchand, R. T., Wood, R., and McCoy, I. L.: Coalescence Scavenging Drives Droplet Number  
761 Concentration in Southern Ocean Low Clouds, *Geophys. Res. Lett.*, 49, e2022GL097819,  
762 <https://doi.org/10.1029/2022GL097819>, 2022.





- 763 Kang, L., Marchand, R. T., and Wood, R.: Stratocumulus Precipitation Properties over the Southern Ocean  
764 Observed from Aircraft during the SOCRATES campaign, ESS Open Archive.,  
765 <https://doi.org/10.22541/essoar.169290579.91095731/v1>, 2023.
- 766 Lu, C., Zhu, L., Liu, Y., Mei, F., Fast, J. D., Pekour, M. S., Luo, S., Xu, X., He, X., Li, J., and Gao, S.:  
767 Observational study of relationships between entrainment rate, homogeneity of mixing, and cloud  
768 droplet relative dispersion, *Atmos. Res.*, 293, 106900,  
769 <https://doi.org/10.1016/j.atmosres.2023.106900>, 2023.
- 770 Lu, M.-L., Sorooshian, A., Jonsson, H. H., Feingold, G., Flagan, R. C., and Seinfeld, J. H.: Marine  
771 stratocumulus aerosol-cloud relationships in the MASE-II experiment: Precipitation susceptibility  
772 in eastern Pacific marine stratocumulus, *J. Geophys. Res.-Atmos.*, 114,  
773 <https://doi.org/10.1029/2009JD012774>, 2009.
- 774 McComiskey, A., Feingold, G., Frisch, A. S., Turner, D. D., Miller, M. A., Chiu, J. C., Min, Q., and  
775 Ogren, J. A.: An assessment of aerosol-cloud interactions in marine stratus clouds based on surface  
776 remote sensing, *J. Geophys. Res.-Atmos.*, 114, <https://doi.org/10.1029/2008JD011006>, 2009.
- 777 McFarquhar, G. M., Bretherton, C. S., Marchand, R., Protat, A., DeMott, P. J., Alexander, S. P., Roberts,  
778 G. C., Twohy, C. H., Toohey, D., Siems, S., Huang, Y., Wood, R., Rauber, R. M., Lasher-Trapp,  
779 S., Jensen, J., Stith, J. L., Mace, J., Um, J., Järvinen, E., Schnaiter, M., Gettelman, A., Sanchez, K.  
780 J., McCluskey, C. S., Russell, L. M., McCoy, I. L., Atlas, R. L., Bardeen, C. G., Moore, K. A., Hill,  
781 T. C. J., Humphries, R. S., Keywood, M. D., Ristovski, Z., Cravigan, L., Schofield, R., Fairall, C.,  
782 Mallet, M. D., Kreidenweis, S. M., Rainwater, B., D'Alessandro, J., Wang, Y., Wu, W., Saliba, G.,  
783 Levin, E. J. T., Ding, S., Lang, F., Truong, S. C. H., Wolff, C., Haggerty, J., Harvey, M. J.,  
784 Klekociuk, A. R., and McDonald, A.: Observations of Clouds, Aerosols, Precipitation, and Surface  
785 Radiation over the Southern Ocean: An Overview of CAPRICORN, MARCUS, MICRE, and  
786 SOCRATES, *B. Am. Meteorol. Soc.*, 102, E894-E928, [https://doi.org/10.1175/BAMS-D-20-](https://doi.org/10.1175/BAMS-D-20-0132.1)  
787 0132.1, 2021.



- 788 Olfert, J. S., Kulkarni, P., and Wang, J.: Measuring aerosol size distributions with the fast integrated  
789 mobility spectrometer, *Journal of Aerosol Science*, 39, 940-956,  
790 <https://doi.org/10.1016/j.jaerosci.2008.06.005>, 2008.
- 791 Painemal, D. and Zuidema, P.: Assessment of MODIS cloud effective radius and optical thickness  
792 retrievals over the Southeast Pacific with VOCALS-REx in situ measurements, *J. Geophys. Res.-*  
793 *Atmos.*, 116, <https://doi.org/10.1029/2011JD016155>, 2011.
- 794 Painemal, D., Chang, F. L., Ferrare, R., Burton, S., Li, Z., Smith Jr, W. L., Minnis, P., Feng, Y., and  
795 Clayton, M.: Reducing uncertainties in satellite estimates of aerosol–cloud interactions over the  
796 subtropical ocean by integrating vertically resolved aerosol observations, *Atmos. Chem. Phys.*, 20,  
797 7167-7177, [10.5194/acp-20-7167-2020](https://doi.org/10.5194/acp-20-7167-2020), 2020.
- 798 Painemal, D., Spangenberg, D., Smith Jr, W. L., Minnis, P., Cairns, B., Moore, R. H., Crosbie, E.,  
799 Robinson, C., Thornhill, K. L., Winstead, E. L., and Ziemba, L.: Evaluation of satellite retrievals of  
800 liquid clouds from the GOES-13 imager and MODIS over the midlatitude North Atlantic during the  
801 NAAMES campaign, *Atmos. Meas. Tech.*, 14, 6633-6646, [10.5194/amt-14-6633-2021](https://doi.org/10.5194/amt-14-6633-2021), 2021.
- 802 Pinsky, M. B. and Khain, A. P.: Turbulence effects on droplet growth and size distribution in clouds—  
803 A review, *Journal of Aerosol Science*, 28, 1177-1214, [https://doi.org/10.1016/S0021-](https://doi.org/10.1016/S0021-8502(97)00005-0)  
804 [8502\(97\)00005-0](https://doi.org/10.1016/S0021-8502(97)00005-0), 1997.
- 805 Pruppacher, H. R. and Klett, J. D.: *Microphysics of clouds and precipitation*, Kluwer Academic Publishers,  
806 Dordrecht, the Netherlands, 1997.
- 807 Sanchez, K. J., Roberts, G. C., Diao, M., and Russell, L. M.: Measured Constraints on Cloud Top  
808 Entrainment to Reduce Uncertainty of Nonprecipitating Stratocumulus Shortwave Radiative  
809 Forcing in the Southern Ocean, *Geophys. Res. Lett.*, 47, e2020GL090513,  
810 <https://doi.org/10.1029/2020GL090513>, 2020.



- 811 Sorooshian, A., Feingold, G., Lebsock, M. D., Jiang, H., and Stephens, G. L.: On the precipitation  
812 susceptibility of clouds to aerosol perturbations, *Geophys. Res. Lett.*, 36,  
813 <https://doi.org/10.1029/2009GL038993>, 2009.
- 814 Terai, C. R., Wood, R., Leon, D. C., and Zuidema, P.: Does precipitation susceptibility vary with  
815 increasing cloud thickness in marine stratocumulus?, *Atmos. Chem. Phys.*, 12, 4567-4583,  
816 [10.5194/acp-12-4567-2012](https://doi.org/10.5194/acp-12-4567-2012), 2012.
- 817 Twohy, C. H., Petters, M. D., Snider, J. R., Stevens, B., Tahnk, W., Wetzel, M., Russell, L., and Burnet,  
818 F.: Evaluation of the aerosol indirect effect in marine stratocumulus clouds: Droplet number, size,  
819 liquid water path, and radiative impact, *J. Geophys. Res.-Atmos.*, 110,  
820 <https://doi.org/10.1029/2004JD005116>, 2005.
- 821 vanZanten, M. C., Stevens, B., Vali, G., and Lenschow, D. H.: Observations of Drizzle in Nocturnal  
822 Marine Stratocumulus, *J. Atmos. Sci.*, 62, 88-106, <https://doi.org/10.1175/JAS-3355.1>, 2005.
- 823 Wang, J., Wood, R., Jensen, M. P., Chiu, J. C., Liu, Y., Lamer, K., Desai, N., Giangrande, S. E., Knopf,  
824 D. A., Kollias, P., Laskin, A., Liu, X., Lu, C., Mechem, D., Mei, F., Starzec, M., Tomlinson, J.,  
825 Wang, Y., Yum, S. S., Zheng, G., Aiken, A. C., Azevedo, E. B., Blanchard, Y., China, S., Dong,  
826 X., Gallo, F., Gao, S., Ghate, V. P., Glienke, S., Goldberger, L., Hardin, J. C., Kuang, C., Luke, E.  
827 P., Matthews, A. A., Miller, M. A., Moffet, R., Pekour, M., Schmid, B., Sedlacek, A. J., Shaw, R.  
828 A., Shilling, J. E., Sullivan, A., Suski, K., Veghte, D. P., Weber, R., Wyant, M., Yeom, J.,  
829 Zawadowicz, M., and Zhang, Z.: Aerosol and Cloud Experiments in the Eastern North Atlantic  
830 (ACE-ENA), *B. Am. Meteorol. Soc.*, 103, E619-E641, [10.1175/BAMS-D-19-0220.1](https://doi.org/10.1175/BAMS-D-19-0220.1), 2022.
- 831 Wang, Y., Zhao, C., McFarquhar, G. M., Wu, W., Reeves, M., and Li, J.: Dispersion of Droplet Size  
832 Distributions in Supercooled Non-precipitating Stratocumulus from Aircraft Observations Obtained  
833 during the Southern Ocean Cloud Radiation Aerosol Transport Experimental Study, *J. Geophys.*  
834 *Res.-Atmos.*, 126, e2020JD033720, <https://doi.org/10.1029/2020JD033720>, 2021a.



- 835 Wang, Y., Zheng, G., Jensen, M. P., Knopf, D. A., Laskin, A., Matthews, A. A., Mechem, D., Mei, F.,  
836 Moffet, R., Sedlacek, A. J., Shilling, J. E., Springston, S., Sullivan, A., Tomlinson, J., Veghte, D.,  
837 Weber, R., Wood, R., Zawadowicz, M. A., and Wang, J.: Vertical profiles of trace gas and aerosol  
838 properties over the eastern North Atlantic: variations with season and synoptic condition, *Atmos.*  
839 *Chem. Phys.*, 21, 11079-11098, 10.5194/acp-21-11079-2021, 2021b.
- 840 Wang, Y., Zheng, X., Dong, X., Xi, B., Wu, P., Logan, T., and Yung, Y. L.: Impacts of long-range  
841 transport of aerosols on marine-boundary-layer clouds in the eastern North Atlantic, *Atmos. Chem.*  
842 *Phys.*, 20, 14741-14755, 10.5194/acp-20-14741-2020, 2020.
- 843 Wang, Y., Zheng, X., Dong, X., Xi, B., and Yung, Y. L.: Insights of warm-cloud biases in Community  
844 Atmospheric Model 5 and 6 from the single-column modeling framework and Aerosol and Cloud  
845 Experiments in the Eastern North Atlantic (ACE-ENA) observations, *Atmos. Chem. Phys.*, 23,  
846 8591-8605, 10.5194/acp-23-8591-2023, 2023.
- 847 Wallace, J. M. and Hobbs, P. V.: *Atmospheric Science: An Introductory Survey*, 2nd edn., Academic  
848 Press/Elsevier, 483 pp, 2006.
- 849 Wood, R.: Drizzle in Stratiform Boundary Layer Clouds. Part I: Vertical and Horizontal Structure, *J.*  
850 *Atmos. Sci.*, 62, 3011-3033, 10.1175/JAS3529.1, 2005.
- 851 Wood, R.: Rate of loss of cloud droplets by coalescence in warm clouds, *J. Geophys. Res.-Atmos.*, 111,  
852 <https://doi.org/10.1029/2006JD007553>, 2006.
- 853 Wood, R., Wyant, M., Bretherton, C. S., Rémillard, J., Kollias, P., Fletcher, J., Stemmler, J., de Szoeko,  
854 S., Yuter, S., Miller, M., Mechem, D., Tselioudis, G., Chiu, J. C., Mann, J. A. L., O'Connor, E. J.,  
855 Hogan, R. J., Dong, X., Miller, M., Ghate, V., Jefferson, A., Min, Q., Minnis, P., Palikonda, R.,  
856 Albrecht, B., Luke, E., Hannay, C., and Lin, Y.: Clouds, Aerosols, and Precipitation in the Marine  
857 Boundary Layer: An Arm Mobile Facility Deployment, *B. Am. Meteorol. Soc.*, 96, 419-440,  
858 10.1175/BAMS-D-13-00180.1, 2015.



- 859 Wu, P., Dong, X., and Xi, B.: A Climatology of Marine Boundary Layer Cloud and Drizzle Properties  
860 Derived from Ground-Based Observations over the Azores, *J. Climate*, 33, 10133-10148,  
861 10.1175/JCLI-D-20-0272.1, 2020.
- 862 Wu, P., Dong, X., Xi, B., Liu, Y., Thieman, M., and Minnis, P.: Effects of environment forcing on marine  
863 boundary layer cloud-drizzle processes, *J. Geophys. Res.-Atmos.*, 122, 4463-4478,  
864 <https://doi.org/10.1002/2016JD026326>, 2017.
- 865 Wyant, M. C., Bretherton, C. S., Wood, R., Blossey, P. N., and McCoy, I. L.: High Free-Tropospheric  
866 Aitken-Mode Aerosol Concentrations Buffer Cloud Droplet Concentrations in Large-Eddy  
867 Simulations of Precipitating Stratocumulus, *Journal of Advances in Modeling Earth Systems*, 14,  
868 e2021MS002930, <https://doi.org/10.1029/2021MS002930>, 2022.
- 869 Zawadowicz, M. A., Suski, K., Liu, J., Pekour, M., Fast, J., Mei, F., Sedlacek, A. J., Springston, S.,  
870 Wang, Y., Zaveri, R. A., Wood, R., Wang, J., and Shilling, J. E.: Aircraft measurements of aerosol  
871 and trace gas chemistry in the eastern North Atlantic, *Atmos. Chem. Phys.*, 21, 7983-8002,  
872 10.5194/acp-21-7983-2021, 2021.
- 873 Zheng, G., Wang, Y., Wood, R., Jensen, M. P., Kuang, C., McCoy, I. L., Matthews, A., Mei, F.,  
874 Tomlinson, J. M., Shilling, J. E., Zawadowicz, M. A., Crosbie, E., Moore, R., Ziemba, L., Andreae,  
875 M. O., and Wang, J.: New particle formation in the remote marine boundary layer, *Nature*  
876 *Communications*, 12, 527, 10.1038/s41467-020-20773-1, 2021.
- 877 Zheng, X., Dong, X., Ward, D. M., Xi, B., Wu, P., and Wang, Y.: Aerosol-Cloud-Precipitation  
878 Interactions in a Closed-cell and Non-homogenous MBL Stratocumulus Cloud, *Adv. Atmos. Sci.*,  
879 39, 2107-2123, 10.1007/s00376-022-2013-6, 2022a.
- 880 Zheng, X., Xi, B., Dong, X., Wu, P., Logan, T., and Wang, Y.: Environmental effects on aerosol–cloud  
881 interaction in non-precipitating marine boundary layer (MBL) clouds over the eastern North  
882 Atlantic, *Atmos. Chem. Phys.*, 22, 335-354, 10.5194/acp-22-335-2022, 2022b.

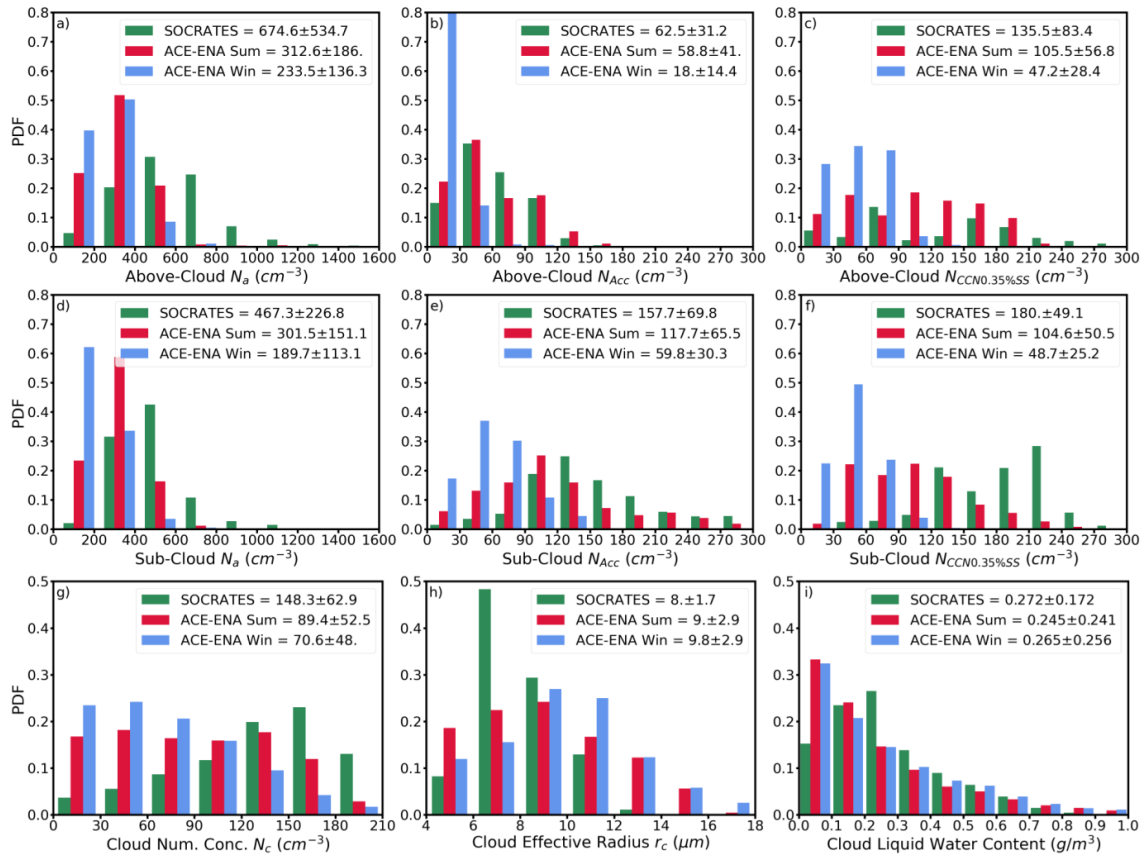


**Figure 1.** Probability Density Functions (PDFs) of  $N_a$ ,  $N_{ACC}$  and  $N_{CCN0.35\%}$  in the above-cloud (a, b, c) and sub-cloud (d, e, f) regimes; and the cloud microphysical properties of  $N_c$  (g),  $r_c$  (h), and  $LWC_c$  (f) within cloud layer. ACE-ENA summer, winter and SOCRATES are color-coded with red, blue and green, respectively.

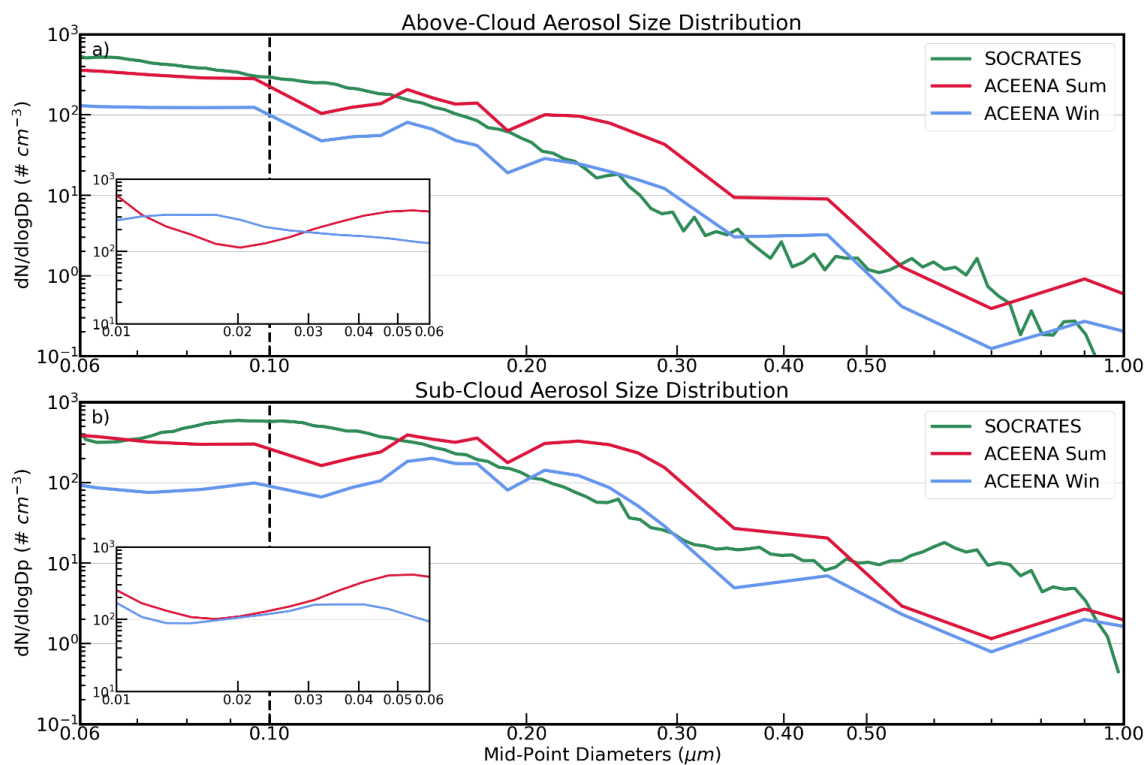


**Figure 2.** Aerosol size distributions ( $D_p = 0.06 - 1 \mu\text{m}$ ) for above-cloud (a) and sub-cloud (b) regimes. The vertical dashed line at  $D_p = 0.1 \mu\text{m}$  denotes the demarcation between Accumulation mode and Aitken mode. The inner plots denote the Aitken mode size distribution ( $D_p = 0.06 - 1 \mu\text{m}$ ) from ACE-ENA. ACE-ENA summer, winter and SOCRATES are color-coded with red, blue and green, respectively.

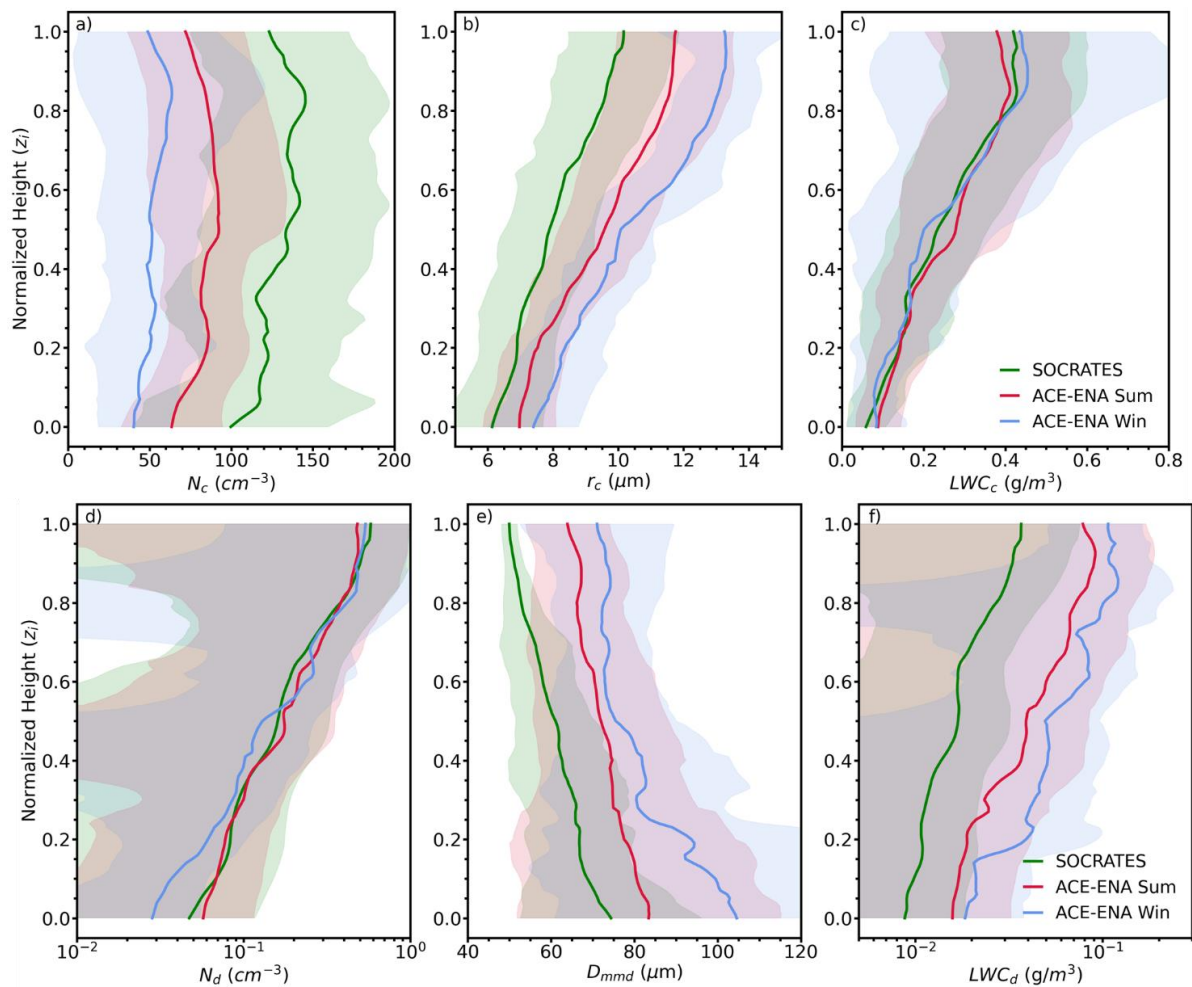


**Figure 3.** Vertical distributions of  $N_c$  (a),  $r_c$  (b),  $LWC_c$  (c),  $N_d$  (d),  $D_{mmd}$  (e), and  $LWC_d$  (f). Here the  $z_i = 0$  denotes cloud base and  $z_i = 1$  denotes cloud top.



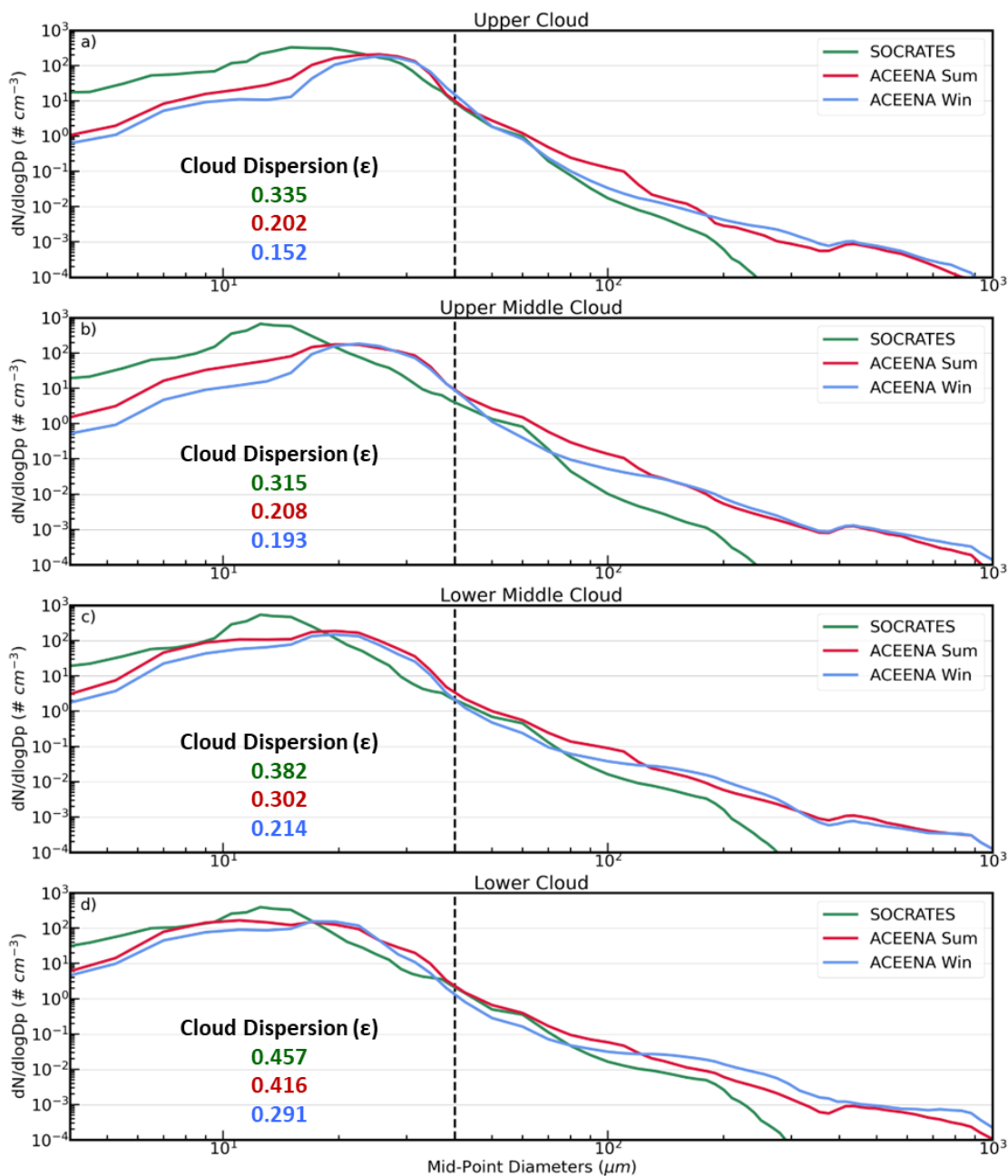


**Figure 4.** Cloud and drizzle size distributions for a) upper cloud ( $z_i > 0.8$ ), b) upper-middle cloud ( $0.5 \leq z_i < 0.8$ ), c) lower-middle cloud ( $0.2 \leq z_i < 0.5$ ) and d) lower cloud ( $z_i < 0.2$ ). The vertical dashed line at  $D_p = 40 \mu\text{m}$  denotes the demarcation between cloud droplets and drizzle drops. ACE-ENA summer, winter and SOCRATES are color-coded with red, blue and green, respectively.

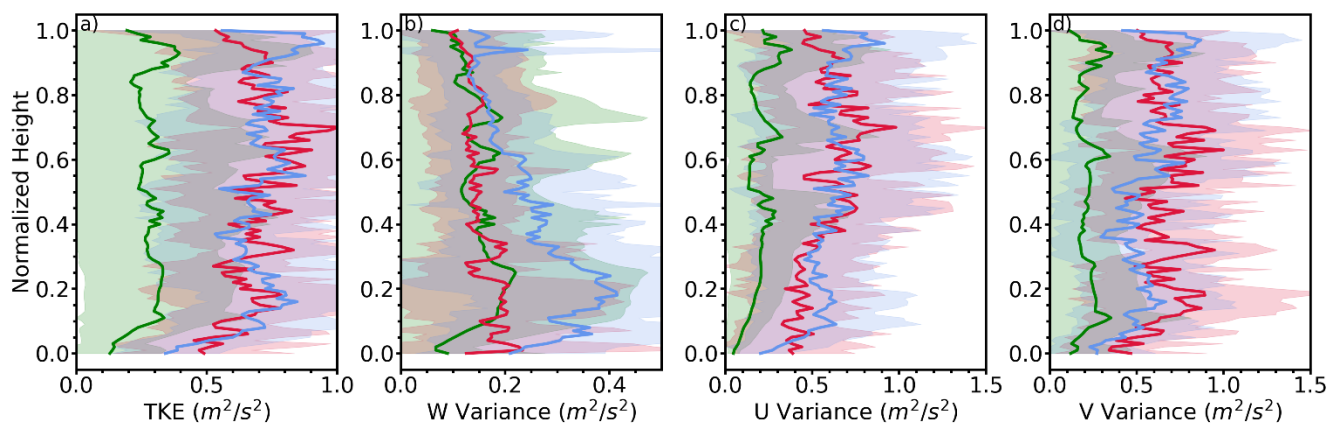


**Figure 5.** Vertical distributions of in-cloud  $TKE$  (a),  $w'^2$  (b),  $u'^2$  (c) and  $v$  (d). ACE-ENA summer, winter and SOCRATES are color-coded with red, blue and green, respectively.

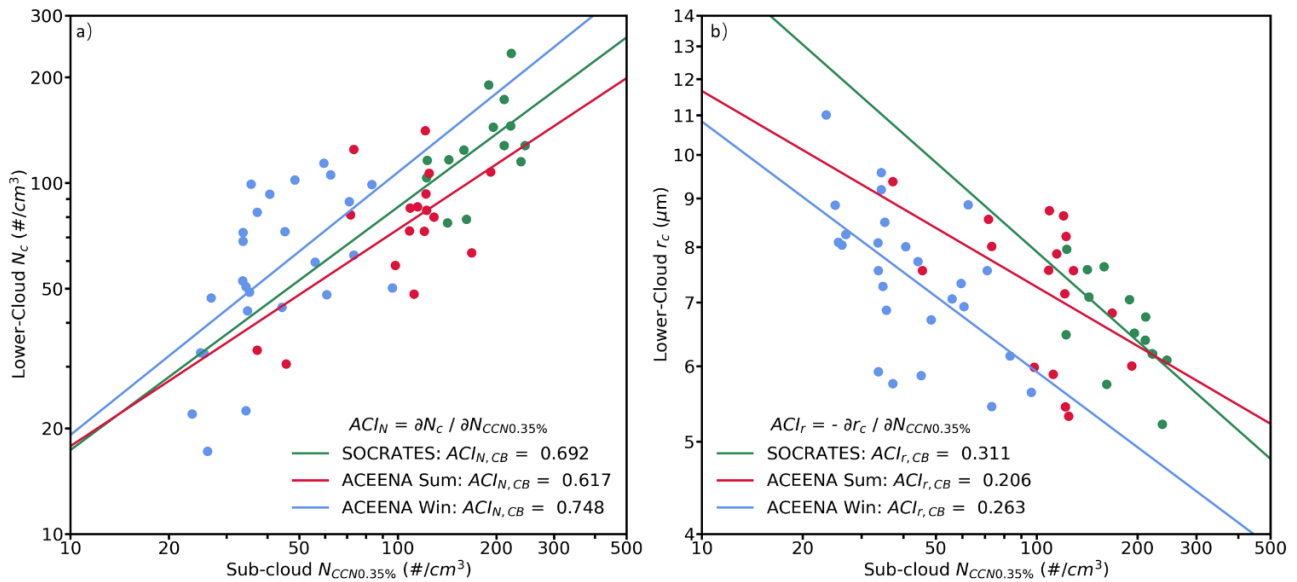


**Figure 6.** Scatterplots of the a)  $N_c$  and b)  $r_c$  at the lower-cloud ( $z_i < 0.2$ ) against the sub-cloud  $N_{CCN0.35\%}$ . ACE-ENA summer, winter and SOCRATES are color-coded with red, blue and green, respectively.

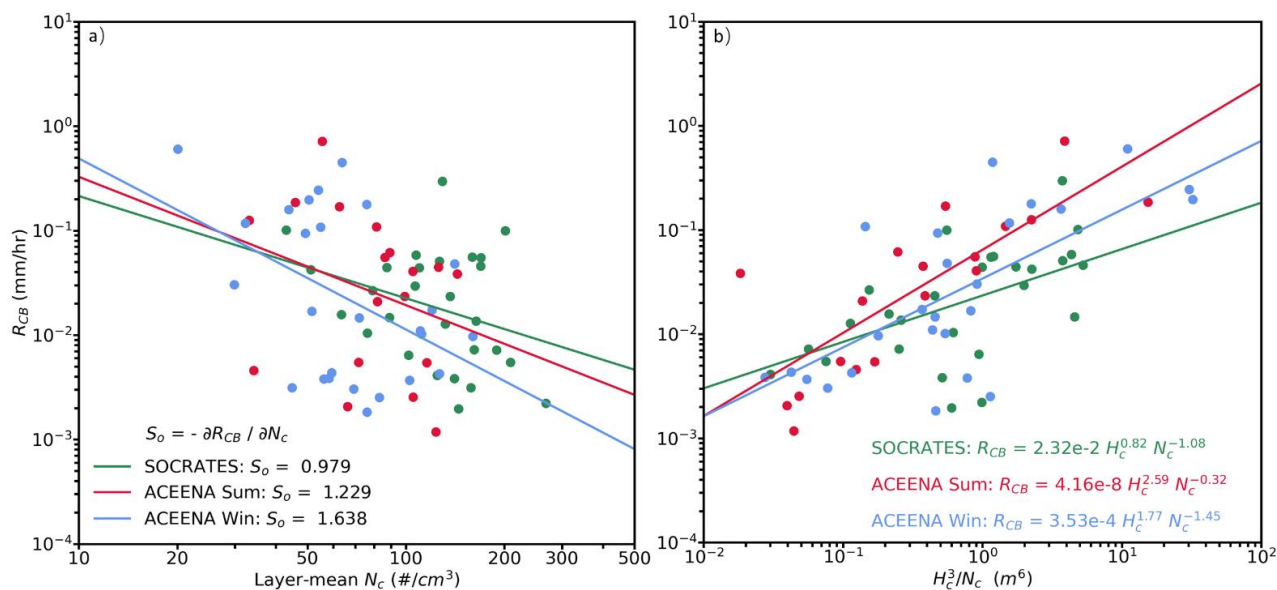


**Figure 7.** Scatterplots of the cloud base precipitation rate  $R_{CB}$  against the a) layer-mean  $N_c$  and b)  $H_c^3/N_c$ . ACE-ENA summer, winter and SOCRATES are color-coded with red, blue and green, respectively.

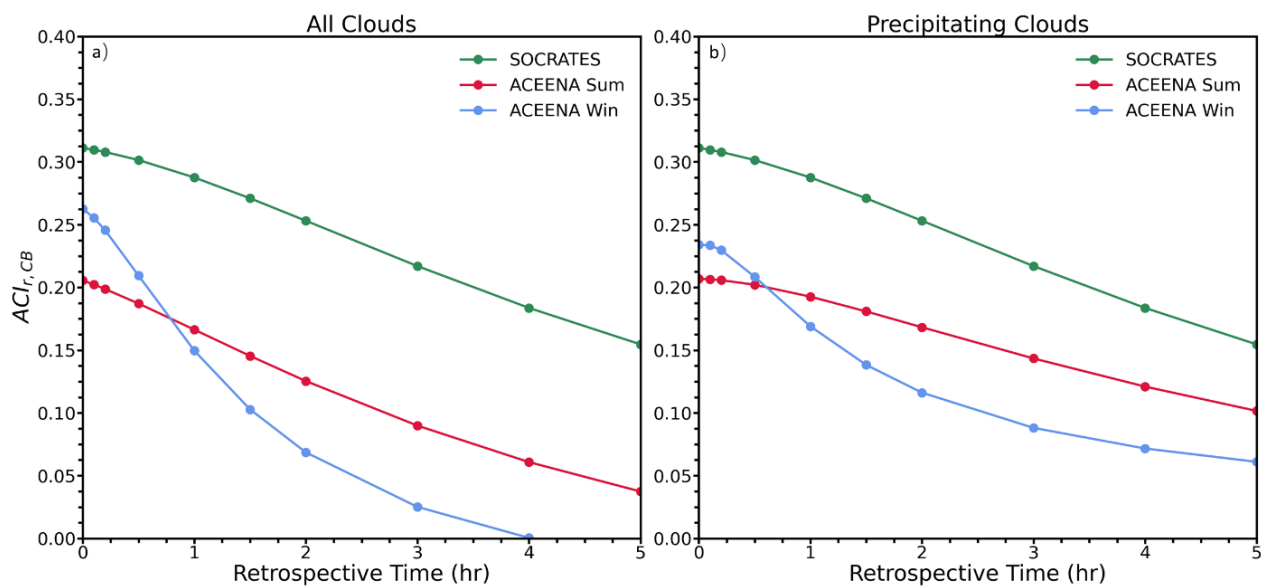


**Figure 8.**  $ACI_{r,CB}$  as a function of the sub-cloud  $N_{CCN0.35\%}$  retrospective time for a) all clouds and b) precipitating clouds.